JGR Atmospheres

Special Section:
SOUTHTRAC-GW: An airborne field campaign to explore gravity wave dynamics at the world's strongest hotspot

Key Points:

- Moderate-to-severe clear air turbulence (CAT) over the Southern Andes is analyzed using 100 Hz in situ data obtained during a flight of the Southern Hemisphere Transport, Dynamics, and Chemistry campaign
- Vertical propagation of mountain waves in the lee of the Southern Andes is recognized as the main source for the turbulence observed
- Anisotropy due to thermal stratification results in turbulent patches within the CAT region with non-Kolmogorov turbulence scaling

Correspondence to:

A. Dörnbrack,
andreas.doernbrack@dlr.de

Not All Clear Air Turbulence Is Kolmogorov—The Fine-Scale Nature of Atmospheric Turbulence

Paola Rodriguez Imazio[1,2] ⓘ, Pablo D. Mininni[3,4] ⓘ, Alejandro Godoy[2] ⓘ, Nicolás Rivaben[2], and Andreas Dörnbrack[5] ⓘ

[1]Consejo Nacional de Investigaciones Científicas y Técnicas, Buenos Aires, Argentina, [2]Servicio Meteorológico Nacional, Buenos Aires, Argentina, [3]Facultad de Ciencias Exactas y Naturales, Departamento de Física, Ciudad Universitaria, Universidad de Buenos Aires, Buenos Aires, Argentina, [4]Instituto de Física del Plasma (INFIP), CONICET—Universidad de Buenos Aires, Ciudad Universitaria, Buenos Aires, Argentina, [5]DLR Oberpfaffenhofen, Institut für Physik der Atmosphäre, Weßling, Germany

Abstract We study a strong clear air turbulence (CAT) event experienced by the German High-Altitude Long-Range research aircraft (HALO) during the Southern Hemisphere Transport, Dynamics, and Chemistry campaign. HALO encountered CAT leeward of the southern Andes Mountains, where tropospheric airflow favored vertically propagating mountain waves that were refracted southeastward into the core of tropopause jet. Turbulence is quantified using spectral quantities and structure functions computed from in situ 100 Hz flight level data. The detected CAT region exhibits strong patchiness, characterized by separated bursts in turbulent kinetic energy and energy dissipation rate. The high resolution in situ observations reveal different turbulent scaling within each patch, in both spectra and structure functions, and following Monin and Yaglom's conversion law. One patch follows power laws with exponents -1.71 ± 0.06, -1.771 ± 0.006, and -1.56 ± 0.05 for the velocity components w, v, and u, respectively, while another patch has exponents -2.17 ± 0.12, -2.50 ± 0.08, and -1.92 ± 0.09. These patches are mediated by a third patch with less clear scaling. While the patches can deviate from Kolmogorov scaling due to the anisotropy of the airflow, they still display evidence of CAT with enhanced energy dissipation rates.

Plain Language Summary Clear air turbulence (CAT) is a common phenomenon in upper layers of the atmosphere, often triggered by the instability of internal gravity waves or by strong wind shear. CAT can be disruptive for airplanes and uncomfortable for pilots and passengers. Nevertheless, the relationship between CAT formation and the resulting strength of bumpiness experienced by an aircraft is not fully understood. Most of these turbulent regions are patchy and exhibit sudden inhomogeneous bursts of velocity and temperature variations. However, CAT is often quantified using spectral quantities assuming isotropic and homogeneous turbulence. Here, we present a case study of a CAT event observed in the lowermost stratosphere during a research flight in the lee of the Andes Mountains near the Drake Passage in South America. The unique 100 Hz high resolution in situ observations allow the study of individual patches within the turbulent event. Their statistical properties can deviate significantly from those of homogeneous and isotropic turbulence, indicating thermal stratification as an important parameter determining the spectral response.

1. Introduction

Clear air turbulence (CAT) is a phenomenon that occurs in the upper troposphere and lower stratosphere (UTLS) and which is not associated with clouds and thunderstorms (Gultepe et al., 2019; Mazon et al., 2018). The unexpected and difficult-to-predict occurrence of this elusive phenomenon is hazardous to aviation, as it is neither visible to pilots nor detectable by standard on-board radars (Sharman et al., 2012). A well-known source for CAT generation is wind shear, mainly produced in the negative shear zone above the atmospheric jet streams (Ellrod et al., 2003; Panofsky et al., 1968; Watkins & Browning, 1973). In the thermally stable stratified airflow, wind shear creates regions of low Richardson number, Ri, where unstable Kelvin-Helmholtz waves can grow and eventually develop into turbulence (Lane et al., 2012). Other important sources of CAT include loss of geostrophic balance in highly curved jet streams (Williams et al., 2003, 2005, 2008), and airflow over mountains, which excites vertically propagating gravity waves (GWs) that become unstable and break (Bramberger et al., 2018; Doyle et al., 2005; Lilly, 1978; McCann, 2001). In particular, GWs-CAT-related events are believed to be more

severe (Bramberger et al., 2020; Schmid & Dörnbrack, 1999; Wilms et al., 2020) and to cover larger horizontal and vertical ranges.

Despite the overall knowledge of CAT, the dynamics underlying the relation between CAT generation processes and its fine-scale nature remains elusive. On one hand, numerical prediction models fail to reproduce all the scales involved in the atmospheric turbulent motions. On the other hand, adequate detection of CAT requires measurements at scales smaller than 1 km with high temporal resolution that are generally not available through standard ground-based and airborne observation networks. Given the multiple scales involved and the risk of actually encountering strong CAT, measurements remain technically challenging and are sparse. The scarcity of airborne observations increases as one moves to higher southern latitudes where there are very few in situ measurements poleward of 55°S, especially in the UTLS region and above, for example, Tuck et al. (1989), Parish and Bromwich (1989), and Carli et al. (2000). Early airborne campaigns were primarily driven by ozone research (Tuck, 2021; Tuck et al., 1997), but also recorded mesoscale temperature variations (Gary, 2008), gravity waves (Bacmeister et al., 1990), and turbulence (Tuck, 2008).

The South American land mass extends to about 55°S. In particular, the Southern Patagonia region, the Drake Passage, and the Antarctic Peninsula are likely to create favorable atmospheric conditions for CAT development due to the combination of strong upper-level fronts associated with frequent storms and strong air currents over the Andes and Antarctandes—a hotspot for gravity wave excitation and propagation. Enhanced vertical transport of momentum and trace gases across the polar night jet stream produced during turbulent events is also relevant to explain the physics underlying the influence of stratospheric ozone depletion in the variability of the Southern Annular Mode (SAM), see for example, Ferreira et al. (2015), Holland et al. (2017), and Jucker and Goyal (2022).

As remarked in Ellrod et al. (2003) and references therein, CAT events are bursty. However, most of the reported CAT events lack direct evidence of their fine-scale patchy nature. Moreover, the appearance of bursts or patches, in the theory of turbulence often called external, large-scale, or on-off intermittency depending on the particular context, seems to be inconsistent with regard to the usual conception of CAT as locally homogeneous Kolmogorov turbulence. Recent studies presented in Rodriguez Imazio et al. (2022) analyze the appearance of a turbulent patch close to a CAT encounter using aircraft measurements of the wind velocity sampled at 10 Hz over the Drake Passage. The CAT event described there exhibits a global Kolmogorov-like nature. Other examples can be found in Bramberger et al. (2018, 2020), where two different CAT encounters with similar measurements are presented. In all these previous studies, turbulent parameters calculated using spectral methods, such as the turbulent kinetic energy (TKE) and the energy dissipation rate ϵ, have well-defined maxima indicating moderate-to-severe turbulence. For determining ϵ these studies assume a $-5/3$ spectral slope, as it is common in this context (Smalikho, 1997).

Dörnbrack et al. (2022) analyzed over 120 hours of 10 Hz airborne vertical wind observations in the UTLS and determined the slope of the log-log spectra from them. They found a mean value of -1.66824, that is, it deviated by less than 0.1% from the phenomenological value $-5/3$ of a Kolmogorov spectrum. However, the slope distribution is rather broad and has a variance of 0.92, that is, about 66% of all observed values fall into the range $-5/3 \pm 0.92$. Only about 8% of all observed values fall into the narrow range where deviation from the phenomenological value is less than 5%. As mentioned by Dörnbrack et al. (2022), "the assumption of an inertial spectrum is often only a crude approximation in determining ϵ" based on spectral methods. Thus, it is noteworthy to investigate the occurrence of non-Kolmogorov turbulence, and to determine how reliable estimates of CAT can be made that supersede the methods commonly used, for example, by Sharman et al. (2014), Bramberger et al. (2020), and Rodriguez Imazio et al. (2022).

Using aircraft data, Mahrt (1989) showed that turbulence in the atmospheric boundary layer may develop as patches of eddies with large intervening areas of low turbulent activity. In that work, a structure functions approach was used to analyze the presence of global and small-scale intermittency in different atmospheric scenarios, arguing that the existence of a global $-5/3$ spectral slope provides limited information on whether turbulence is homogeneous or not, as well as on other flow properties.

Recent results from direct numerical simulations (DNS) discussed in Rorai et al. (2014), Feraco et al. (2018), and Marino et al. (2022) show that stably stratified flows are likely to develop long-lasting bursts that become more intense with stronger thermal stratification in a range of parameters in terms of the Froude and buoyancy Reynolds numbers. The appearance of such patches has been attributed to a strong correlation between the vertical velocity and the potential temperature, that is, by the presence of internal gravity waves. Inside these patches, characterized
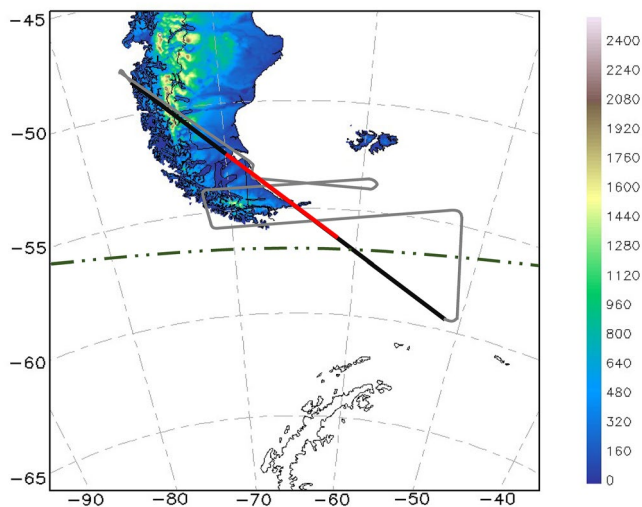
Figure 1. HALO's total flight path of research flight ST08 on 11 September 2019 in gray, thick back, and thick red. The black and red sections are superimposed and mark the selected northwest-southeast flight segments considered in this study (referred to as leg 2), with the red line highlighting the turbulence segment where HALO encountered clear air turbulence (CAT). The region with blue background denotes the southernmost continental region of WRF-SMN operational domain with topographic elevations in m. The double-dotted-dashed line is the southernmost boundary of the WRF-SMN operational domain.

through the global Froude number, energetic bursts at scales comparable to that of the mean flow may arise, being powerful enough to modify the spectral distribution of the energy; see, for instance, Mahrt (1989), Alexandrova et al. (2008), Pearson and Fox-Kemper (2018), and Chau et al. (2021) for similar examples of bursts in homogeneous turbulence in the atmosphere, in the solar wind, and in the ocean. This phenomenon is known as large-scale intermittency, and for the case of stably stratified flows it was suggested to be characterized by a transition in the spectrum of the vertical velocity from a $k^{-5/3}$ to a k^{-2} inertial range scaling (from more isotropic to more stratified bursts) in Marino et al. (2022). Since the statistics of the flow deviate greatly from Gaussian due to the occurrence of bursts, it is expected that the time series of kurtosis will to some extent reflect the patchy nature of the flow, see Mahrt (1989), Rorai et al. (2014), Feraco et al. (2018), and Marino et al. (2022).

In this work, we study a strong GW-CAT event experienced by the German High-Altitude Long-Range research aircraft (HALO) during the Southern Hemisphere Transport, Dynamics, and Chemistry (SOUTHTRAC) campaign (Rapp et al., 2021). The event occurred in the lee of the southernmost Andes mountains at the entrance to the Drake Passage. Our aim is to characterize the observed turbulent airflow using both spectral methods and structure functions, combining campaign measurements with numerical forecast data. We show that CAT and the flow properties associated with vertically propagating mountain waves have a pronounced patchy character, as indicated by the appearance of individual bursts of spectral quantities calculated from in situ data, such as TKE and ϵ. Sections with large ϵ can develop within the CAT region, even if the scaling of turbulence differs from the Kolmogorov scaling.

The rest of the paper is organized as follows. Section 2 introduces the data set and methods. Section 3 describes the meteorological situation. Section 4 presents the spectral analysis of the aircraft data, and the calculation of TKE and ϵ. Spectral results are also contrasted with the results of the structure function approach to determine ϵ, characteristic scales, and flow properties. Section 5 discusses the results and, finally, Section 6 summarizes the results and concludes the paper.

2. Methods and Data

The turbulence analysis presented is based on airborne measurements from HALO research flight ST08, see Figure 1 for the complete flight path. HALO departed from Rio Grande, Argentina, at 23:00 UTC on 11 September 2019, heading northwest toward the Chilean coast, crossing part of the Andes. After a turn over the Pacific Ocean, HALO headed southeast toward the Drake Passage. This flight segment will be referred to as leg 2 according to Table S1 in Dörnbrack et al. (2022), see the black line in Figure 1. On both cross-mountain legs, the Rayleigh lidar aboard HALO observed mountain wave-induced polar stratospheric clouds directly over the Andes at around 23:45 UTC and at 01:15 UTC on 12 September 2019, respectively (Dörnbrack et al., 2020). The CAT event occurred afterward in the lee of the Andes between 01:20 UTC and 02:00 UTC, see the red line in Figure 1.

The 2,047 km long leg 2 was flown at FL400 ($\approx$180 hPa) with a southeasterly heading and passed over the Southern Andes region of Argentine Patagonia and the Drake Passage. At flight level, the wind direction changed gradually from west-southwest to west-northwest and the horizontal wind $V_H = \sqrt{u^2 + v^2}$ increased poleward; in average V_H was about 37 m s^{-1}, see Figures 2a and 2b. The mean relative humidity along the flight leg was below 5% and no clouds were observed at flight level, so the turbulence encountered in the middle of leg 2 can therefore be called CAT. This CAT event is characterized by large amplitudes in the vertical wind and potential temperature profiles, see Figures 2c and 2d.

The in situ observations used for Figure 2 are from the Basic HALO Measurement and Sensor System (BAHAMAS), which measures atmospheric parameters at flight level with a sampling frequency of 1 Hz. To investigate the turbulence event in more detail, the high-frequency 10 and 100 Hz BAHAMAS data are analyzed (Giez et al., 2017, 2021). The higher resolution BAHAMAS data at 100 Hz is only available for specific sections of the
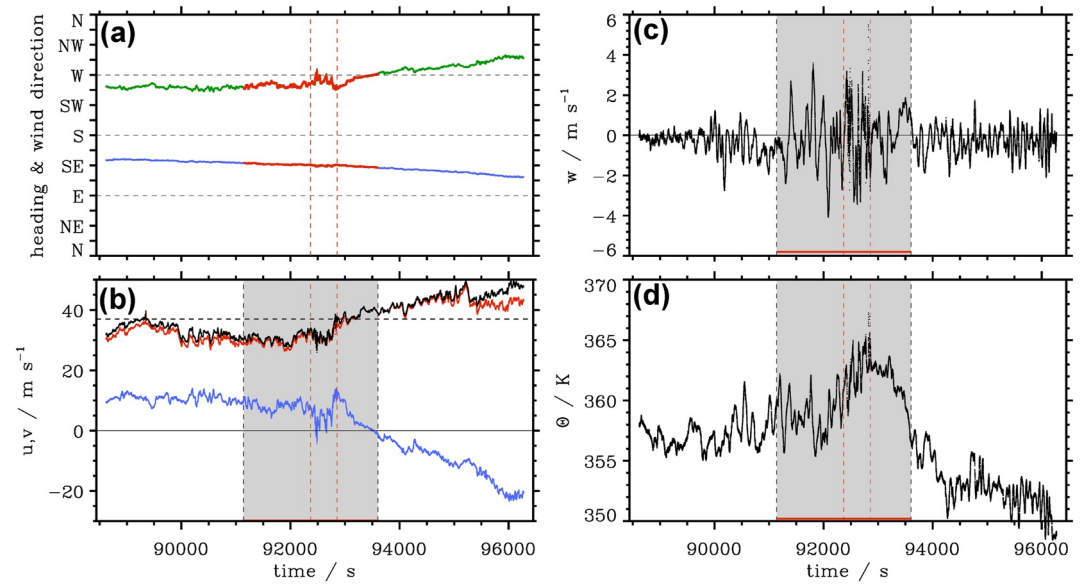
Figure 2. Time series (as function of UTC time starting at 00 UTC on 11 September 2019) of various quantities along leg 2 of HALO's research flight ST08. (a) Wind direction (green line) and HALO's heading (blue line). The red segments mark the period of the studied turbulence event. (b) Zonal (red) and meridional (blue) wind components, and horizontal wind V_H in black. (c) Vertical wind and (d) potential temperature. The gray-shaded areas mark the period of the studied turbulence event and the red dashed vertical lines enclose the turbulence segment as analyzed in Section 4. Data: 1 Hz BAHAMAS data.

flight route, which, in this case, cover the entire segment of the CAT encounter, shaded in gray in Figure 2. For the remainder of the subsection, 10 Hz data are used for supplemental description.

Two methods are employed to analyze this dataset. The first is based on the characterization of turbulence parameters using spectral methods. The second aims at obtaining a complementary description of the CAT event with a more direct interpretation of the scales involved, using velocity structure functions. To complement these measurements, NWP models are employed to determine the time, location, and the large-scale flow patterns responsible for the CAT event.

2.1. Spectral Methods

In this case study, we use two quantities to characterize atmospheric turbulence at flight level: the specific turbulent kinetic energy (TKE) and the cube root of the energy dissipation rate (EDR = $\epsilon^{1/3}$), using similar methods to those presented in Bramberger et al. (2018).

TKE is determined mainly by the large energy-containing eddies, whereas ϵ is defined as the rate of conversion of the turbulent kinetic energy into thermal energy taking place at the small scales. The two quantities together can provide a very useful description of CAT encounter, and they are commonly used for determining turbulence intensity in aviation. In particular, EDR can be directly related to aircraft-specific loads and therefore calibrated with respect to different aircraft types (Cornman, 2016; Cornman et al., 1995; MacCready, 1964; Sharman et al., 2014). The respective thresholds for light, moderate, and severe turbulence used as a reference here follow those proposed by Sharman et al. (2014).

The TKE per unit mass is calculated according to

$$\text{TKE} = \frac{1}{2}\left(\sigma_{\text{uac}}^2 + \sigma_{\text{vac}}^2 + \sigma_{\text{w}}^2\right),\tag{1}$$

where uac and vac denote the horizontal wind components along and across the flight route, respectively, and w

is the vertical wind; from here on this vector is u_i = (uac, vac, w). The variances $\sigma_i = \sqrt{\overline{u_i'^2}} = \sqrt{\overline{\left(u_i - \overline{u_i}\right)^2}}$ are calculated for different sublegs that are between 4 and 16 km long, where the overbar denotes the mean over the respective subleg interval.

The energy dissipation rate ϵ is calculated on the basis of the inertial dissipation technique according to Champagne ([1978](#)), Piper and Lundquist ([2004](#)), and Večenaj et al. ([2012](#)). In this approach, the Kolmogorov prediction for the turbulent energy spectrum (from here on, K41; Kolmogorov, [1941a](#)) is considered, and the energy dissipation rate is obtained from the power spectral energy density (PSD) S_i, assumed to be

$$S_i(k) = C_i \epsilon_i^{2/3} k^{-5/3} \equiv \text{PSD}_i \tag{2}$$

where the subscript i refers to the respective wind component u_i, k is the horizontal wavenumber, and $C_i = \{0.53, 0.707, 0.707\}$ are the Kolmogorov constants (Oncley et al., [1996](#); Piper & Lundquist, [2004](#); Strauss et al., [2015](#)). Following Equation [2](#), EDR is calculated according to

$$\text{EDR}_i = \epsilon_i^{1/3} = \left[\frac{\overline{S_i(k)k^{5/3}}}{C_i} \right]^{1/2} \tag{3}$$

Note the determination of EDR assumes the CAT event follows K41 scaling. Despite this limitation, EDR is useful for identifying regions of strong dissipation, although the true energy dissipation rate may be overestimated if the spectrum is steeper than the K41 scaling. An independent method of estimating the energy dissipation rate will be provided in Section [4.2.2](#).

EDR values shown in the present study are obtained as follows: the complete flight leg is divided into 4 km sublegs, and the individual spectra computed in these sublegs are averaged over the whole leg. Spectra on each of these 4 km sublegs are calculated using Welch's method (Welch, [1967](#)). In this manner, each subleg is divided into three overlapping segments, where a Tukey window is applied, and the spectral energy density is calculated with a fast Fourier transform. From the resulting spectrum, Equation [3](#) is then used to calculate the EDR$_i$ values along the flight path. Details of the spectral method algorithm can be found in Appendix [A](#).

2.2. Structure Functions

We calculate second and third-order velocity structure functions of order p for the velocity component u_i as

$$Sp_{u_i}(l) = \langle [u_i(x + l) - u_i(x)]^p \rangle = \langle [\delta u_i(l)]^p \rangle \tag{4}$$

where l is a separation distance along the x (flight)-direction and the angle brackets denote an ensemble average (Lesieur, [1993](#); Monin & Yaglom, [1975](#)). According to Monin and Yaglom ([1975](#)), for a given power law l^β of the structure function, the spectral representation of this power law should be converted as k^α, with the spectral index $\alpha = -(1 + \beta)$ for $-3 < \alpha < -1$, see also Essenwanger and Reiter ([1969](#), Equation 9). From here, it follows that the second-order structure function $S2$ provides a measure of the turbulent kinetic energy in physical space at different scales (strictly speaking, the structure function evaluated at the scale l corresponds to energy in scales $r < l$, with a small contribution from the eddies larger than l, see Davidson ([2022](#))). For a Kolmogorov spectrum (Gottlieb & Orszag, [1977](#)) the power law in physical space should be

$$S2 = C_2 \, \epsilon^{2/3} \, l^\beta \quad \text{with} \quad \beta = 2/3 \tag{5}$$

where C_2 is a constant that takes different values for transverse and longitudinal structure functions.

It has been argued that third-order structure functions may be more useful to characterize atmospheric turbulence (Cho & Lindborg, [2001](#); Koch et al., [2005](#); Lindborg, [1999](#); Wacławczyk et al., [2020](#)). First, they circumvent the arbitrariness of the constant in Equation [5](#), and second, they provide the direction of the energy flux as either a downward or upward cascade, which also allows a direct estimate of the turbulent energy dissipation rate. Here we will calculate the mixed third-order structure functions,

$$S3(l) = \left\langle |\delta\mathbf{u}|^2 \delta u_{ac} \right\rangle = -\frac{4}{3} \epsilon \, l^\gamma \tag{6}$$

where $\mathbf{u}$ is the wind velocity vector in the aircraft-related coordinate system and γ is the scaling index whose theoretical value is $\gamma = 1$. The right-hand side of Equation [6](#), known as the 4/3rd law, is a direct consequence of Kolmogorov's 4/5th law (Antonia et al., [1997](#), [2019](#); Kolmogorov, [1941a](#), [1941b](#)). Note that while Equation [6](#) is often derived in the context of isotropic and homogeneous turbulence, rigorous derivations can be obtained for stratified flows (Augier et al., [2012](#)). In that context, ϵ is the energy dissipation rate of the kinetic energy, and

other relations can be computed to estimate the dissipation rate of potential energy, as well as the exchange rate between kinetic and potential energy. The formal derivation in Augier et al. (2012) also implies that the value of ϵ in a stratified flow may depend on the large-scale flow conditions.

In practice, when dealing with observations, the ensemble averages in Equations 4 and 6 are replaced by time averages using Taylor hypothesis (Frisch, 1995), and velocity increments for each wind component are calculated independently from the in situ measurements. In this sense, calculations follow the approach used in Cho et al. (2003). Increments l are defined in terms of time intervals τ, as $l = u_a \tau$, where u_a is the mean air speed over the considered sublegs.

2.3. NWP Models

The synoptic situation during the research flight is described using global as well as regional NWP models. First, the ECMWF's ERA5 reanalysis data (Hersbach et al., 2020) are used to characterize the synoptic situation. This data set is produced using 4D-VAR data assimilation and model forecasts by the ECMWF's Integrated Forecast System (IFS) cycle CY41R2 with 137 hybrid model levels in the vertical and the model top located at 0.01 hPa. In addition, six-hourly operational analyses and short-term forecasts at 1-hr resolution of the IFS are used to generate two-dimensional curtains of meteorological variables. This operational IFS has a higher spatial resolution than ERA5 and is also used to compute vertical derivatives at flight level to characterize the vertical shear of the horizontal wind

$$S = \sqrt{\left(\frac{\partial U}{\partial z}\right)^2 + \left(\frac{\partial V}{\partial z}\right)^2}$$

where U and V are the model outputs for the zonal and meridional wind components, and the Brunt-Väisälä frequency,

$$N = \sqrt{\frac{g}{\Theta} \frac{\partial \Theta}{\partial z}}$$

where Θ is the model output for the potential temperature. In our study, these outputs are interpolated onto the flight track to describe the evolution of both quantities at flight level at and around the CAT event.

To describe mesoscale features of the atmospheric flow, we use high-resolution simulations of the WRF model from the operational forecasts of the Argentine National Meteorological Service (Servicio Meteorológico Nacional, SMN) (Skabar et al., 2018). This model is used for operational purposes and for atmospheric dynamics research (Powers et al., 2017). At SMN, this model is implemented in its 4.0 version with the Advanced Research dynamic core (WRF-ARW) (Skamarock & Klemp, 2008). The implementation includes four daily forecast cycles, initialized at 00, 06, 12, and 18 UTC, all for a period of 48 hr, producing forecasts on an hourly basis. They are initialized from the forecasts of the NCEP Global Forecast System (GFS) with a horizontal resolution of $0.25° \times 0.25°$. Boundary conditions are incorporated hourly. Operational model configuration corresponds to a single domain of $1,000 \times 1,250 \times 38$ grid points, equivalent to approximately 4 km horizontal resolution and 38 vertical pressure levels, with the top at 50 hPa. The whole domain covers latitudes between 15°S and 60°S and longitudes between 80°W and 50°W. The time step employed is 40 s Figure 1 shows the southernmost region of the domain covered by the WRF-SMN operational model (blue background).

Parameterizations used include: cloud microphysics scheme WSM6 (WRF single—moment 6—class microphysics scheme) (Hong & Lim, 2006), the Mellor-Yamada-Janjic (MYJ) scheme for the planetary boundary layer (Janić, 2001), RRTM for longwave radiation (Mlawer et al., 1997), the Dudhia scheme for shortwave (Dudhia, 1989), and the NOAH soil model with four layers that reach 2 m depth (Mukul Tewari et al., 2004). Convection is not parameterized and solved explicitly in the runs.

3. CAT Event

3.1. Synoptic Analysis

The overall atmospheric situation during this period in early September 2019 was described in Dörnbrack et al. (2020) and Rapp et al. (2021). Research flight ST08 took place during a minor sudden warming of the stratosphere (SSW), but mountain waves excited due to airflow over the Andes were still able to penetrate to stratospheric
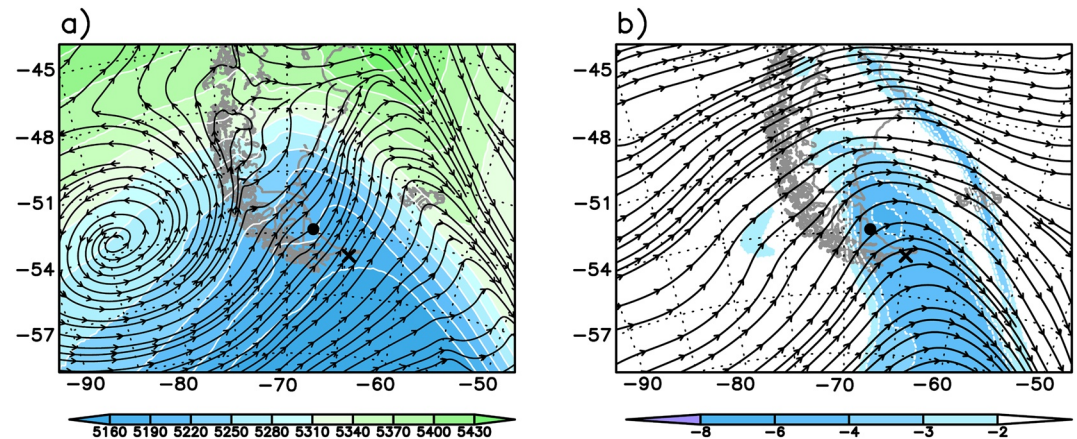
Figure 3. Synoptic conditions on 01:00 UTC for 12 September 2019: (a) Thickness between 1,000 and 500 hPa (gpm, color shaded) and streamlines at 1,000 hPa (black lines). (b) Potential vorticity less than -2 PVU (color shaded, $1 \text{ PVU} = 1 \times 10^{-6} \text{ m}^2 \text{ s}^{-1} \text{ K kg}^{-1}$) and streamlines at 300 hPa (black lines). The black dot at $54°$S represents the location of Rio Grande. The black cross denotes the location of the clear air turbulence (CAT) event at 1:30 UTC identified in BAHAMAS data. Data: ERA5.

heights, see Figures 11 and 12 in Rapp et al. (2021). Responsible for the excitation of the mountain waves was an intense cold front that crossed southern Patagonia on 11 September 2019 and moved quickly toward northeast. The very cold polar air mass reached the island of Tierra del Fuego during the night of 12 September 2019.

Figure 3a illustrates this situation by streamlines at the 1,000 hPa level and the 1,000 to 500 hPa thickness as obtained from ERA5 at 01:00 UTC: The intense high located upstream of the Drake Passage and centered at $53°$S and $87°$W favored a southwesterly flow and the cold air advection near Tierra del Fuego and south of Santa Cruz. At upper levels, an intense and amplified trough with its trough axis located to the east of Tierra del Fuego and extending polewards was present the 300 hPa pressure level, see Figure 3b. The cyclonically curved polar front jet stream increased in strength poleward. A stratospheric air intrusion with large cyclonic potential vorticity (PV) values and a significant PV gradient over the center of Tierra del Fuego Island can also be identified in Figure 3b. It can be assumed that the cyclonic strengthening was related to the shift of the stratospheric polar vortex during the SSW mentioned above.

The change in the wind direction at these levels as indicated by the streamlines in Figure 3 established an airflow over the southern Andes mountains that excited vertically propagating mountain waves. In the time period before the research flight, mountain waves were excited further north close to El Calafate. We refer the reader to Figure 13 of Dörnbrack et al. (2020) for the temporal evolution of the upstream profiles on 11 September 2019 and for glider measurements in the lee waves occurring both in the troposphere (Wildmann et al., 2021) and stratosphere on this day.

The vertical wind at 200 hPa as shown in Figure 4a confirms the existence of mountain waves over the Southern Andes and in the lee over the southernmost region of Tierra del Fuego. These mountain waves are present at all lower levels and in the southern part also at later times (not shown). The leeward phase lines are stretched and elongated toward the southeast close to region where the CAT event occurred at $54°$S and $64.7°$W (see the black cross in Figure 4). Here as well as at higher stratospheric levels, they are refracted into the core of the polar front jet as well as into the polar night jet, see also Figure 13 of Rapp et al. (2021). In this sense, mountain waves are likely to be involved in the modulation of local stratospheric airflow and created a suitable scenario for the development of turbulence, a process already discussed by Panofsky et al. (1968). Turbulence cannot be resolved by the WRF simulations used, but the simulated frontogenesis function defined as the Lagrangian derivative of the horizontal temperature gradient,

$$F = \frac{d}{dt} \nabla_h \Theta \qquad (7)$$

under the influence of the southeastward propagating mountain waves shows increased wave-like thermal gradients in the region where HALO passed through the turbulence region (see Figure 4b).
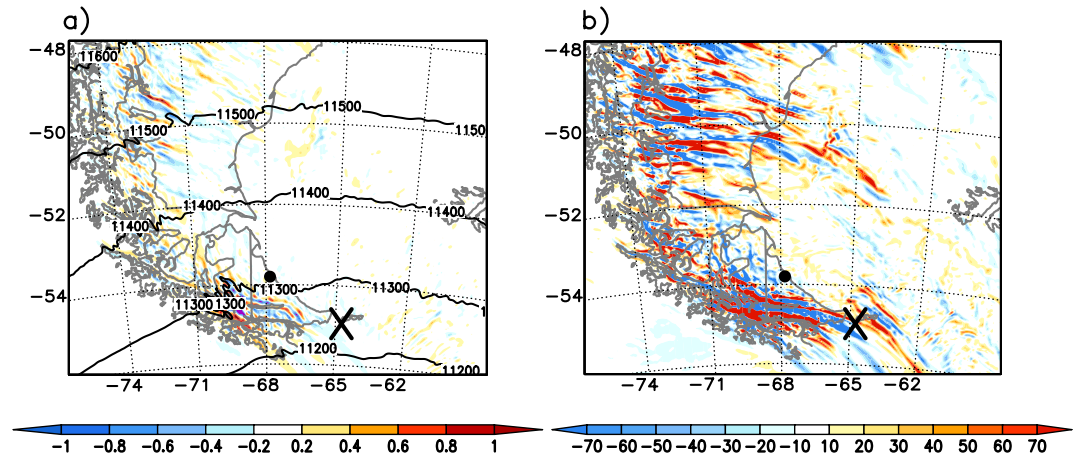
Figure 4. (a) Vertical wind (m s^{-1}, color shaded) and geopotential height (gpm, black lines) at 200 hPa. (b) Frontogenesis function F according to Equation 7 (10^{-9} K m^{-1} s^{-1}, color shaded) at 200 hPa. Both plots are valid at 01:00 UTC on 12 September 2019. The location of the clear air turbulence (CAT) encounter registered by HALO around 01:30 UTC is marked with a black cross, the black dot marks Rio Grande. Data: WRF simulations.

Figure 5 depicts the evolution of the Brunt-Väisälä frequency N and of the vertical shear of the horizontal wind S at HALO's flight level along leg 2 as derived from the operational IFS. The course of N shows a pronounced minimum inside the region where CAT was encountered. From the computed minimum, N increases to common stratospheric values of 0.02 s^{-1} with increasing time, that is, poleward. HALO was here about 3.5 km above the thermal tropopause. The value of S varies inside the leg attributed to the CAT encounter and increases further southwards as HALO approached the core of the polar front jet. Inside the red segment in both panels of Figure 5, the Richardson number never becomes smaller than 5. However, it must be noted that the vertical resolution of the IFS is about 300 m in this altitude range, that is, the magnitude of the vertical derivatives might be underestimated. In spite of these limitations, the simultaneous peaks in S and N are consistent with the behavior that will be described later: a sudden breakdown of background stratification due to wind shear could be associated with the development of patches with different levels of turbulent activity.

3.2. Aircraft Measurements

Figure 6 shows the time series of potential temperature Θ and the three wind velocity components u, v, and w as a function of latitude from the 10 Hz data measured by BAHAMAS between 01:20 UTC and 02:00 UTC, that is, inside the gray-shaded region in Figure 2, or the red segments of Figure 6. The length of this segment is about 655 km and extends from the southern Andes in Argentine Patagonia at around 52.6°S to the Drake Passage at about 56°S, see the red segment in Figure 1. The time series, especially those for Θ and w, clearly show a coexistence of smooth waves and turbulent patches. The variance of the velocity components increases within the turbulent patches by up to a factor of 4 (see Section 4.1).

A wave energy flux analysis, as done in Dörnbrack et al. (2022), reveals a positive vertical wave energy flux $\mathrm{EF}_z \equiv \overline{w'p'}$, averaged over the 655 km section as shown in Figure 6, of 2.43 W m^{-2}, that is, EF_z is about a factor 2 larger than the one for the whole leg 2, see Table S2 in Dörnbrack et al. (2022). Interestingly, the Eliassen-Palm relation is satisfied within 10% as $-\mathbf{u} \cdot \mathbf{MF} = 2.17$ W m^{-2}, where $\mathbf{MF} \equiv (\overline{\rho\,u'w'}, \overline{\rho\,v'w'})$ is the vector of the horizontal momentum flux (Eliassen & Palm, 1960). Additionally, both the meridional as well as the zonal energy fluxes are negative indicating that the
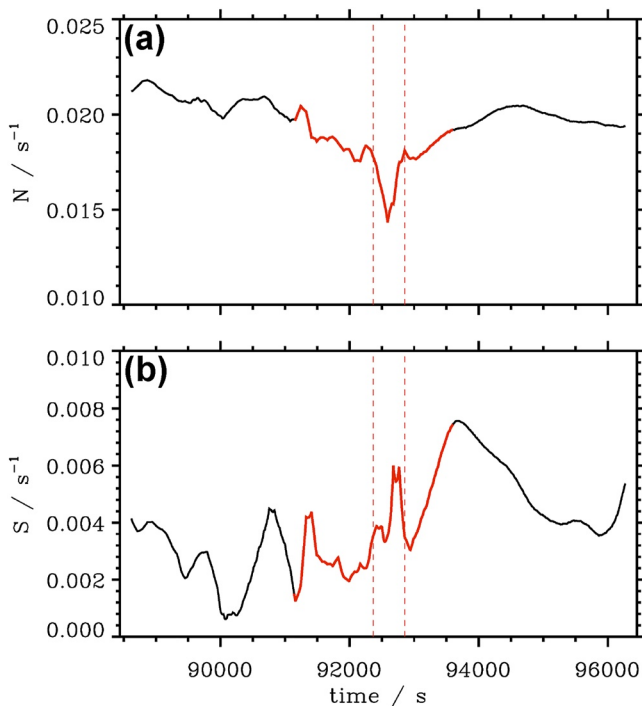

Figure 5. Brunt-Väisälä frequency N (a) and vertical shear of the horizontal wind S (b) along the flight path of leg 2 and interpolated to the flight altitude of HALO. The red segments mark the period of the studied turbulence event. The red dashed lines enclose the turbulence segment as analyzed in Section 4. The Froude number $Fr \equiv V_H/(NL)$ in the red segment is about 0.11 assuming $V_H \approx 37$ m s^{-1}, an average value of $N \approx 0.018$ s^{-1}, and $L \approx 17$ km (the maximum length of each turbulent segment as defined in the text). Data: Operational IFS analyses and short-term forecasts.
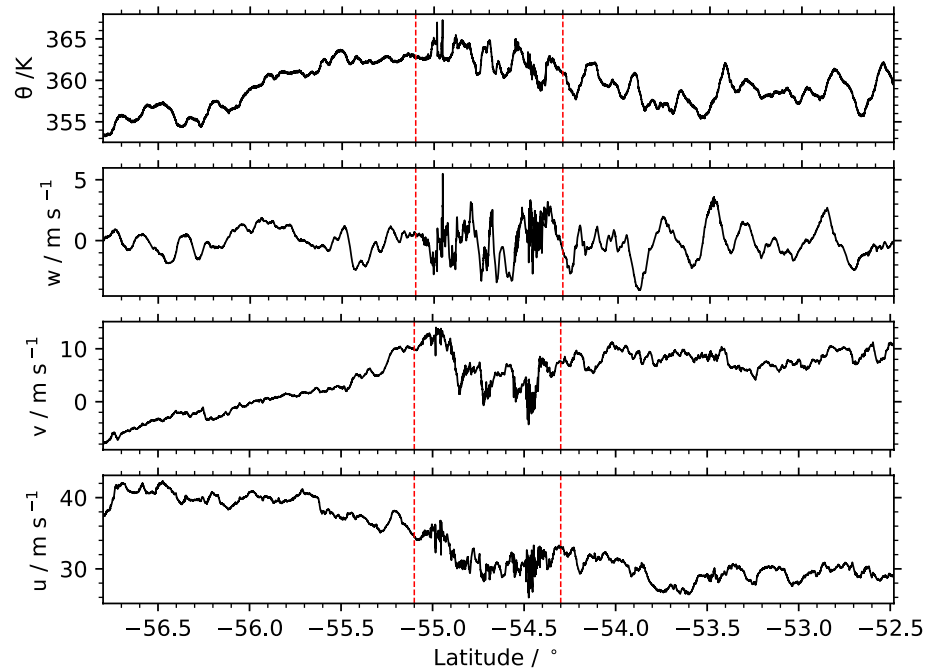
Figure 6. HALO 10 Hz in situ measurements along the gray section as shown in Figure 2 as function of latitude for potential temperature (top), vertical wind (second panel from top), and meridional and zonal wind components, respectively (bottom two panels). Measurements were conducted at FL400, corresponding to an altitude of about 12 km and 180 hPa. Vertical lines mark the boundaries of the turbulence segment where larger variations in the measured quantities occurred over a length of about 127 km.

waves are propagating against the nearly zonal background flow. This means that the vertically upward propagating and almost linear waves are mostly likely mountain waves excited by the flow over the Andes.

Figure 7 shows the binned energy spectra along this leg for the horizontal wind V_H (as defined in Section 2) and the vertical wind component w. These spectra are intended to identify wave modes present in the HALO data. Log-log spectra are presented in 8, see also Dörnbrack et al. (2022, Figure B2). Dominating scales in the vertical wind have horizontal wavelengths of about 30–60 km and at 15 km. As expected, the spectral energy of V_H is dominated by longer horizontal scales $\lambda_x > 100$ km but also shows a maximum between 30 and 40 km. The shorter modes of about 15 km are present both in V_H and w. Consistent with the results of Smith et al. (2016) and Smith and Kruse (2017), it is the medium-length mountain waves that carry the horizontal momentum upward. However, one must be extremely cautious about drawing definitive conclusions about the correctness of our wavelength estimates as it is not known at which angle HALO traversed the gravity wave phase lines; HALO's heading was not aligned with the wind (see Figure 2a) and as suggested by the WRF results (see Figure 4) the mountain waves were refracted into the core of the polar front jet, that is, their wavelengths are overestimated by the HALO observations.

In addition to the smooth waves, small-scale turbulent structures are present in all observed variables in Figure 6, especially in the section between 55°S and 54.3°S, which is about 127 km long (this region is enclosed within the vertical dashed red lines used as a reference in Figure 6). Hereafter, this section of the flight is referred to as the turbulence segment. Here, in situ measurements reveal large peak-to-peak amplitudes for the three wind velocity components u, v, and w as well as a gradual poleward decrease of the potential temperature by about 10 K due to the colder temperature toward the core of the cyclone, see Figure 2d. Also, a strong correlation between the vertical velocity and the potential temperature is observed inside this region, leading to even larger vertical wave energy fluxes of $EF_z = 3.63$ W m^{-2} in comparison to the longer leg discussed before. This means that in the turbulence segment, a coexistence of vertically propagating mountain waves and turbulence is observed. Pilot reports from ST08 confirm HALO's CAT encounter at around 01:30 UTC.

Inside the turbulent region, the vertical velocity w reached peak values of 5.4 m s^{-1} and the zonal wind component u stayed close to 30 m s^{-1} but increased gradually poleward due to the presence of the jet. Interestingly, the
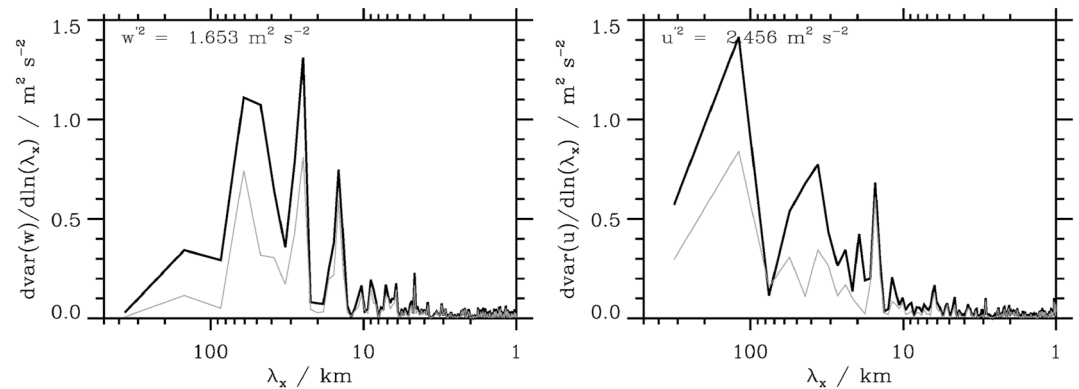
Figure 7. Binned energy spectra for the vertical wind component w (left panel) and the horizontal wind V_H (right panel from the leg as shown in Figure 1) of ST08. Thick black lines are results without tapering window, thin black lines are spectra tapered with a Hanning window. Data: 1 Hz BAHAMAS data interpolated on a regular 250 m grid.

meridional wind v dropped to values below zero inside the turbulent region, indicating strong turbulent mixing in the nearly zonal airflow of about 30 m s^{-1}. The observations of the horizontal velocity components indicate a strongly horizontally sheared airflow in the lower stratosphere. The poleward decrease of Θ is accompanied by a shift in the horizontal wind, where a maximum meridional wind v of about 14.8 m s^{-1} dropped to negative values further south, along with an increase of the zonal wind component u. North of 54.3°S, potential temperature and vertical velocity exhibit wavy patterns, characterized by ridges with an apparent horizontal wavelength of about 50 km (Figure 7) and without superimposed small-scale structures. Peak-to-peak amplitudes in the horizontal wind speed components become very small, and all parameters show smoothly varying quantities suggesting the dominance of vertically propagating mountain waves here. The overall picture of the data analyzed in this section of HALOs research flight ST08 thus suggests a scenario in which two very well-defined, spatially distinct regions can be identified: Apparently longer horizontal waves appear to occur in the north, and shorter ones in the south. These regions are clearly separated by the occurrence of turbulence between 55°S and 54.3°S.

4. Analysis

4.1. Spectral Analysis

Figure 8 shows the power spectral densities (PSD$_i$) as a function of wavenumber k and wavelength λ calculated for the three wind velocity components uac, vac, and w in an aircraft-based coordinate system. Here, the 100 Hz data were used in 4 km overlapping sublegs within the turbulence segment from 55°S to 54.3°S. Note this figure covers the range of 5 m to 5 km, while the spectra in Figure 8 cover a horizontal scale range from 1 to 500 km. A turbulent spectrum with Kolmogorov-like scaling is observed for all velocity components in a wide range of wavenumbers, going from $k \approx 5 \times 10^{-3}$ m^{-1} to $k \approx 5 \times 10^{-1}$ m^{-1}. For larger scales (smaller k), the PSD of uac flattens at scales of the order of 1 km, whereas the PSD for w and vac seem to undergo a wider energy cascade. Approaching smaller scales (larger wavenumbers), some aliasing is observed for the PSDs of uac despite the windowing procedure used in the calculations.

Following previous studies using BAHAMAS measurements at 10 Hz (see, e.g., Bramberger et al., 2018, 2020; Rodriguez Imazio et al., 2022), inertial range scaling was fixed between 0.24 and 5 Hz for all velocity components to compute the eddy dissipation rates ϵ_i from the power spectra according to Equation 3. This choice is a compromise between taking into account as much data as possible with less variance in the spectral slope, but excluding artifacts that could be due to digital noise or aliasing. Following this choice for the inertial range, the spectral slopes were computed through a best fit minimizing the squared error. Values found for the three velocity components within this range of frequencies correspond to $\alpha_w = -1.77 \pm 0.04$, $\alpha_{vac} = -1.88 \pm 0.03$, and $\alpha_{uac} = 1.57 \pm 0.03$. Aliasing may still be responsible for the smaller values obtained for the spectral slope of the uac spectrum, due to an artificial increase of energy content at small scales (see, for instance, Prabhu, 2014). Also, whereas the fixed range of frequencies is based on previous references that used similar data sets, this range of scales is selected heuristically, and energy cascades may develop in shorter or longer ranges than those used. This uncertainty and the piling up of energy caused by aliasing may lead to variations in the spectral slope.
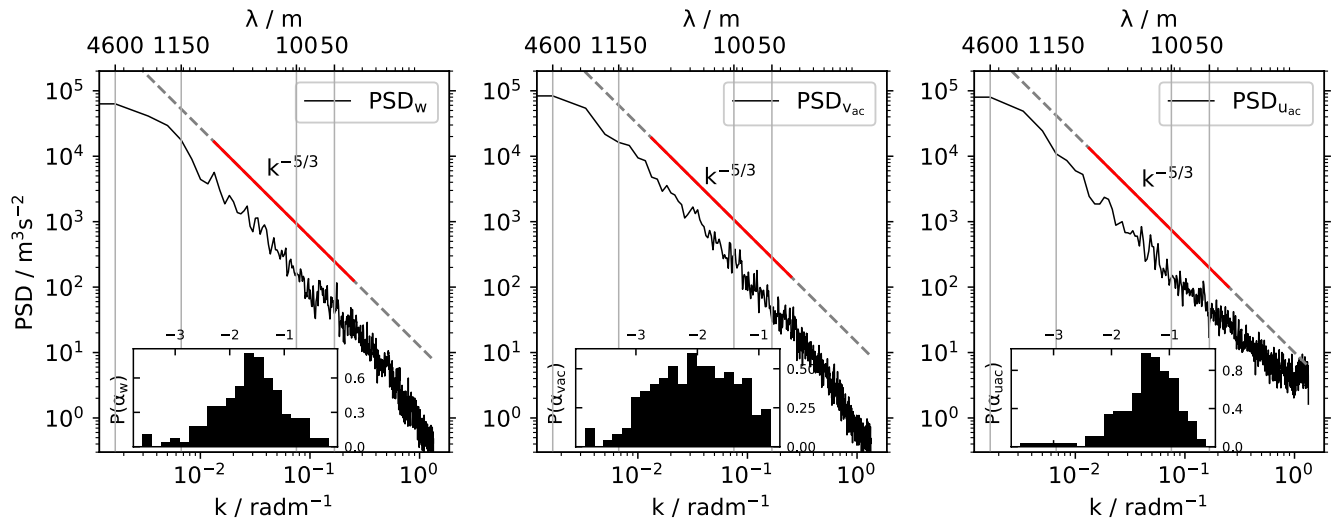
Figure 8. Power spectral density S_i for the vertical and horizontal velocity components in an aircraft-related coordinate system for the entire turbulence segment of 127 km length (black solid line). Kolmogorov scaling is denoted with gray dashed lines as a reference, and subinertial range scaling used for the calculations of the spectral slopes α_i is denoted with red lines, see text. The insets on each panel show the distribution of the spectral slopes α_i obtained from a best fit on individual energy spectra calculated in 4 km sublegs inside the turbulence segment.

Nonetheless, the α-value for uac is similar to the K41 spectrum considering error bars. But this is not the case for the spectral slopes obtained for w and vac, which seem to correspond to a steeper spectrum often associated with turbulence in stratified flows, that is, closer to a spectral slope of -2. Signatures of anisotropy due to thermal stratification can also be observed in Figure 6, where the observed fluctuations seem to change from a more isotropic behavior north of the CAT event to a more anisotropic or more wave-dominated behavior in the south. As will be discussed later, the presence and persistence of a thermally stably stratified airflow leads to the formation of individual patches within the turbulence segment where characteristic quantities, such as the turbulent dissipation, can change compared to the Kolmogorov prediction.

Here, it is important to point out that errors in the spectral slopes (and also those shown in Table 1) are those resulting from the best fit to the averaged spectrum. A detailed explanation of the spectral algorithm used to obtain the α_i values, along with a sensitivity test toward the different choices for the Welch method is given in Appendix A. As an illustration of other sources of variability, insets in Figure 8 show the histograms of the spectral slopes α_i calculated for each of the 4 km subleg spectra inside leg 2. Whereas the distribution of the spectral indices for each velocity component are consistent with the α_i reported in the previous paragraph, it can be seen that the distributions are broad and multimodal. This is more evident for α_{vac}, where the standard deviation of the distribution is ≈ 0.6. Again, as will be discussed below, this multimodal distribution of the spectral indices is consistent with the lack of homogeneity inside the turbulence segment and the presence of patches with different turbulent scaling.

Profiles of TKE and EDR can be obtained from the in situ measurements of the velocity components via the variance and energy spectrum calculations, respectively, as outlined in Section 2. Figure 9a shows the profiles of

Table 1
Spectral Indices (Negative Spectral Slope α_i) and Second-Order and Third-Order Structure Function Indices β and γ According to Equations 5 and 6), Respectively, Calculated for w, uac, and vac in the North, Center, and South Patches of the Turbulence Segment

Segment	$-\alpha_w$	$-\alpha_{\text{vac}}$	$-\alpha_{\text{uac}}$	β_w	β_{vac}	β_{vac}	γ
CAT	1.77 ± 0.04	1.88 ± 0.03	1.57 ± 0.03	0.789 ± 0.008	0.752 ± 0.003	0.760 ± 0.002	0.929 ± 0.002
North	1.71 ± 0.06	1.77 ± 0.06	1.56 ± 0.05	0.650 ± 0.007	0.689 ± 0.004	0.661 ± 0.002	0.973 ± 0.002
Center	1.41 ± 0.06	1.53 ± 0.07	1.33 ± 0.05	0.991 ± 0.008	0.998 ± 0.011	0.528 ± 0.008	1.330 ± 0.012
South	2.17 ± 0.12	2.50 ± 0.08	1.92 ± 0.09	1.078 ± 0.005	1.070 ± 0.010	0.911 ± 0.002	1.045 ± 0.006

Note. For homogeneous isotropic turbulence, the respective values should be $\alpha = -1.666$, $\beta = 0.666$, and $\gamma = 1$, respectively.
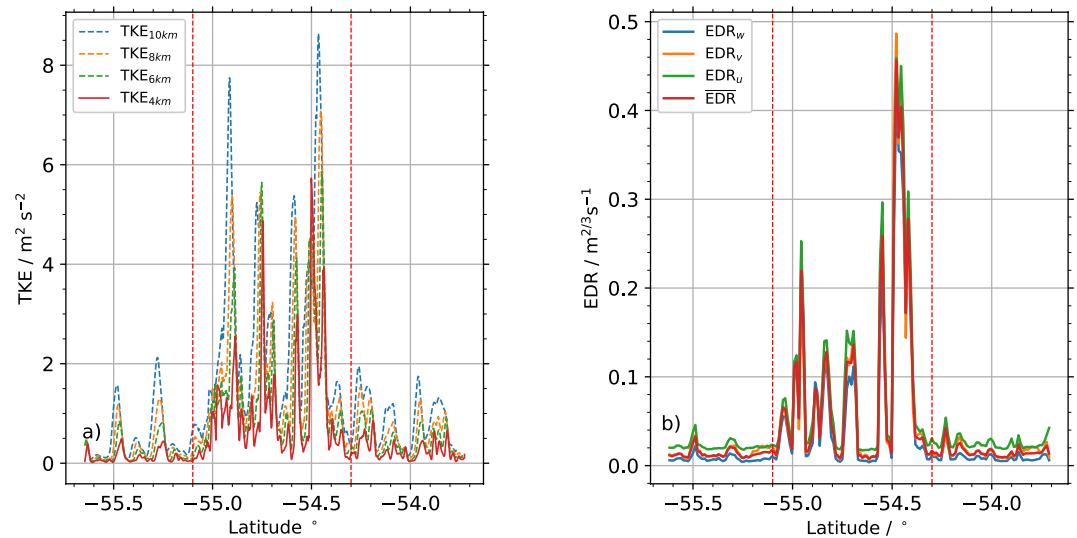
Figure 9. (a) Specific turbulent kinetic energy (TKE) derived from different subleg lengths as indicated by the different colors and line styles, along the flight path. (b) $\text{EDR}_i = \epsilon_i^{1/3}$ for all wind components in an aircraft-related coordinate system and the geometric mean $\overline{\text{EDR}}$ calculated from all wind components, along the flight path.

the TKE as calculated for subleg lengths of 4, 6, 8, and 10 km, respectively. Several peaks can be identified for all subleg lengths. They are located in the turbulence segment as marked by the vertical dashed red lines in Figure 9. In the turbulence segment, TKE is enhanced by a maximum factor of about 8, and a minimum factor of about 5 when compared to the rest of the leg, taking maximum values of 5.8 $\text{m}^2\,\text{s}^{-2}$ for the 4 km subleg, and values above 8 $\text{m}^2\,\text{s}^{-2}$ for the 10 km subleg.

Next, EDR values along the flight path were calculated using Equation 3, and the results are shown in Figure 9b. Since turbulent scales affecting aircraft are in the range of about 300–1,000 m (Bramberger et al., 2020; Hoblit, 1988; MacCready, 1964; Sharman et al., 2014; Vinnichenko, 1980), only curves obtained from the 4 km sublegs are shown. The EDR for uac, vac and w, and their geometric mean $\overline{\text{EDR}}$ show a very similar distribution to that observed for TKE along the flight path, with several bursts of elevated EDR values occurring in the turbulence segment between 55°S and 54.3°S. In comparison with the reference values discussed in Sharman et al. (2014) and references therein, it can be seen that EDR values overcome the threshold for moderate-to-severe turbulence (EDR > 0.2 $\text{m}^{2/3}\,\text{s}^{-1}$) in a large fraction of the patchy CAT encounter. Outside the turbulence segment, both north and south, EDR values become very small and are nearly equal for the three velocity components, indicating calm atmospheric conditions and a more stable and smooth airflow.

As aforementioned, the appearance of these enhanced values of TKE and EDR within the turbulence segment may follow the formation of strongly localized-in-space turbulent patches, as a consequence of the system trying to recover stable thermal stratification. In this sense, the estimation of EDR values from spectral quantities based on Kolmogorov scaling needs to be revised in view of the different nature and scaling laws of stratified turbulent flows. As described in Rorai et al. (2014) and references therein, the patchy nature of stratified turbulence can be characterized in terms of the Froude number $Fr \equiv V_H/(NL)$. In this study, the Froude number estimated from the segments of length L (as will be defined below) and the Brunt-Väisälä frequency N from model data (see Figure 5a) is $Fr \approx 0.11$. This is in good agreement with those reported in Feraco et al. (2018), Marino et al. (2022), and Rorai et al. (2014) for turbulent stratified flows, where strong vertical drafts develop in localized patches with large kurtosis of vertical velocity and potential temperature.

Following this Fr value, patches with extreme EDR or TKE values are likely to occur when turbulence develops. Under these conditions, turbulent mixing inside the CAT region could act to locally break the stable stratification, leading to smaller regions where the flow is less stratified. As indicated by the global energy spectra, stable stratification is not completely broken, leading to scaling laws with spectral slopes ranging between −5/3 according to K41, and those expected for stratified turbulence, that is, −2 or steeper as seen in numerical simulations (Marino et al., 2022).

Moving on to the smaller scales, it remains to be clarified up to which scale mixing is able to break up a stable stratification into smaller patches, and how these patches compare to Kolmogorov theory. This distinction is important because the only estimate of EDR values so far is based on Kolmogorov theory. In practice, if the CAT encounter can be described as smaller CAT patches or bursts according to K41, the problem remains limited by resolution or sampling frequency, but not by theory.

While exploring these issues is beyond the scope of a simple case study, the unique high-resolution measurements at 100 Hz allow a detailed description of the flow in each patch. For this purpose, the turbulence segment was divided into three smaller segments centered around three EDR (and TKE) maxima between 54.3°S and 55°S. These segments are designated as north, center, and south of the CAT event (from right to left in Figure 9) and are located at 54.47°S (north), 54.54°S (center), and 54.95°S (south). The approximate horizontal extent of these three segments (patches) is 17 km (north), 14 km (center), and 12 km (south), respectively.

To investigate the nature of each of the individual patches, the same procedure applied to the whole turbulence segment was applied to each patch. Figure 10 shows the average PSD of w, vac, and uac for each patch (black solid curves), and the individual PSDs for each subleg (gray dotted curves). Since the segments are shorter in the center and south, there is less space available for calculating the spectra, resulting in fewer overlapping sublegs and fewer curves being considered for these patches. From north to south of the turbulent segment (from top to bottom in Figure 10), it can be seen that the spectra of all velocity components undergo an energy cascade with spectral slopes transitioning from $-5/3$ to -2.

North, PSDs of the three wind velocity components (top panels) follow an inertial range scaling close to $k^{-5/3}$ for more than one decade in k-space and in λ between 10 m $< l <$ 1,150 m (this scaling is shown as a reference in the panels). In this patch, inertial range spectral slopes are, within error bars, slightly steeper than $-5/3$ in the case of w and vac (-1.71 ± 0.06 and -1.771 ± 0.006, respectively), whereas the spectral slope for uac is closer to the K41 prediction (-1.56 ± 0.05).

In the central patch (middle panel in Figure 10), the PSDs of w, vac, and uac show a slope closer to a $k^{-5/3}$ scaling law, albeit with less clear scaling of the inertial range, especially for w and vac. In this region, the spectra exhibit bumps and they are more noisy compared to the northern patch, resulting in the inertial range being more difficult to discern. It may be also argued that some spectra display a knee with different behavior at large and small wave numbers. In spite of these limitations, estimates of the spectral slopes α_i denoted with red lines in the middle panels of Figure 10 are $\alpha_w = -1.41 \pm 0.06$, $\alpha_{vac} = -1.53 \pm 0.07$ and $\alpha_{uac} = -1.33 \pm 0.05$.

South of the event (bottom panel in Figure 10), the three wind velocity components exhibit inertial range scaling compatible with $\sim k^{-2}$ or even steeper, within the same range of wavenumbers as in the north and center patches. Here, calculation of spectral slopes yield $\alpha_w = -2.17 \pm 0.12$, $\alpha_{vac} = -2.50 \pm 0.08$ and $\alpha_{uac} = -1.92 \pm 0.09$, for w, vac, and uac, respectively.

In terms of geographic location, these spectra suggest that CAT is more isotropic on the north side of the event, where the spectra follow a scaling law closer to $k^{-5/3}$, and more stratified in the south, where the scaling laws are closer to k^{-2}. Such transitions are similar to those observed in theoretical and numerical studies of stably stratified turbulent flows (Davidson, 2022; Lindborg, 1999; Marino et al., 2022; Rorai et al., 2014), where changes in the level of stratification result in changes in the scaling laws. Also, the spectra are in agreement with the diagnosed poleward increase of the Brunt-Väisäla frequency as shown in Figure 5a, and with the departures from Kolmogorov scaling reported before when the spectrum of the CAT event was considered as a whole. Spectral indices calculated in the inertial range of each patch (denoted with red solid lines on each panel of Figure 10) are listed in the first three columns of Table 1.

4.2. Structure Functions

4.2.1. Second-Order Structure Functions

Figure 1 shows the second-order structure functions of the three velocity components as calculated inside the whole turbulence segment for different sublegs ranging from 4 to 16 km (here, color code denotes the different subleg lengths). The structure functions $S2$ of w, vac and uac in the different sublegs collapse to a single curve with the same scaling. These scaling laws, obtained in the inertial range between $\approx$10 m and $\approx$1,000 m, show good agreement with $S2 \sim l^{\beta}$ with $\beta \approx 0.8$ (see gray dashed lines in Figure 11). For the particular case of w and vac,
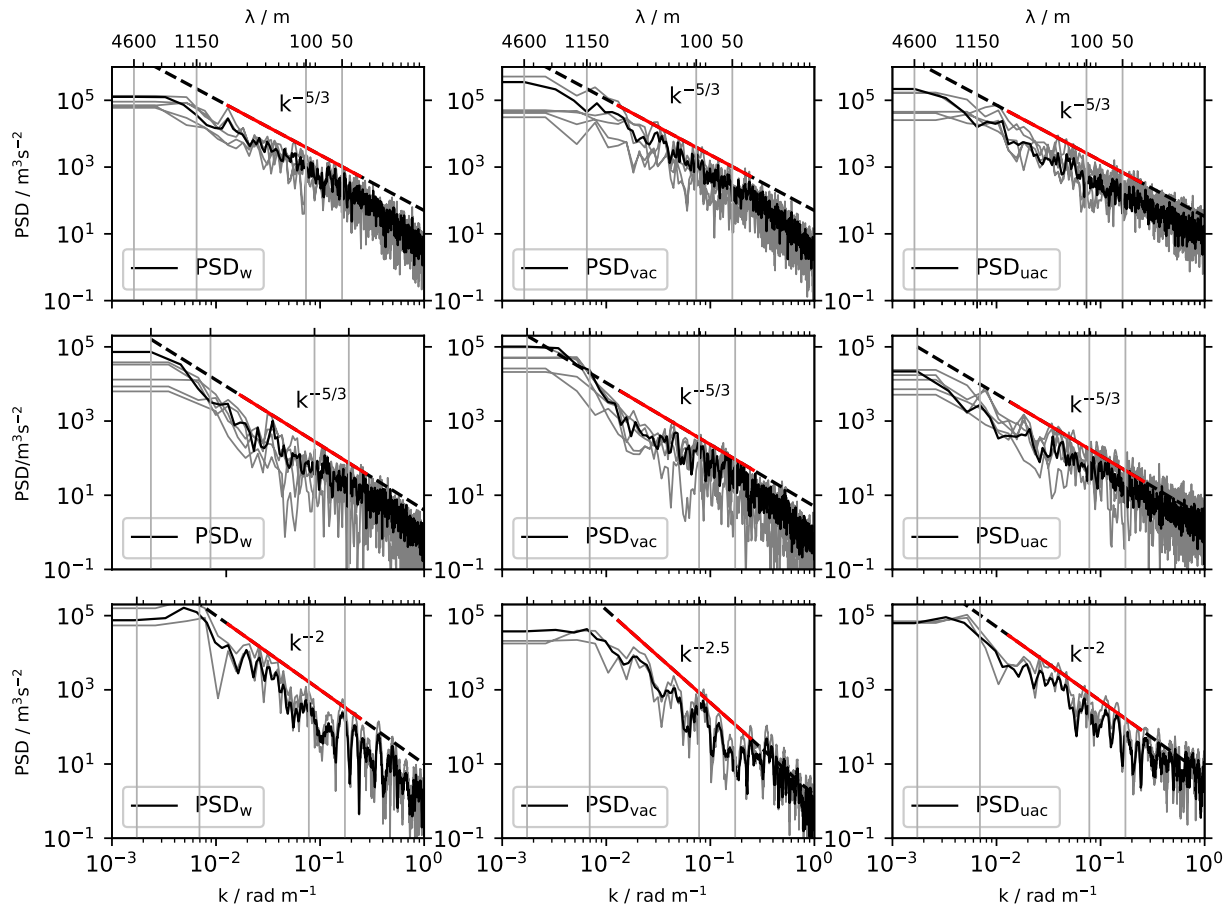
Figure 10. Power spectral density S_i for the three velocity components in an aircraft-related coordinate system w, vac, uac from left to right, on 4 km overlapping sublegs. Top panel shows spectra calculated on the north patch, whereas middle and bottom panels show spectra on the center and south segments, respectively. Inertial range scaling is shown as a reference in gray dashed lines on each panel. Red solid lines denote the extension of the inertial range used for the calculation of the spectral indices α_i.

this value is in very good agreement with the Monin and Yaglom (1975) law applied to the corresponding spectral slopes calculated from their spectra (see Section 2.2), yielding $\alpha = -(1 + \beta) \approx -1.8$, which is compatible with values obtained from a best fit of the inertial range scaling of the w and vac spectra, see Section 4.1 and Table 1. Such a close match cannot be achieved for uac, since the scaling of $S2$ is slightly different from that expected from the corresponding spectrum. As mentioned earlier, the difference can be attributed to aliasing in the data at large frequencies in the spectrum, which results in a slightly flatter spectrum, and therefore in smaller spectral slopes. Calculated values of β for w, vac, and uac using a best fit of the corresponding $S2$ inertial ranges (see solid black lines in Figure 11) are 0.789 ± 0.008, 0.752 ± 0.008, and 0.760 ± 0.002, respectively. These values, along with all indices calculated for the entire turbulence segment and within each patch, are listed in Table 1.

Overall, second-order structure functions in the entire turbulence segment show very similar signatures of stratification comparable to those seen for the energy spectra. Scaling laws of $S2$ calculated for the whole CAT segment depart from the $l^{2/3}$ law expected from K41 theory, and the structure functions are steeper. Note that a scaling $S2 \sim l$ is expected for a k^{-2} scaling law in the corresponding spectra. This departure gives another indication that the entire turbulence segment is not homogeneous, and that analysis of individual patches may provide better agreement with the spectral scaling. Following the procedure described above for examining the individual patches within the turbulence segment, structure functions were calculated for every wind speed component within the north, center, and south patches.

From the spectral slopes suggested by the full straight lines in Figure 10, second-order structure functions in the south patch are expected to exhibit an inertial range scaling closer to $S2 \sim l$, related to a k^{-2}-law in the spectra. On the other hand, $S2$ in the north patch can be expected to follow a scaling law consistent with K41, which gives
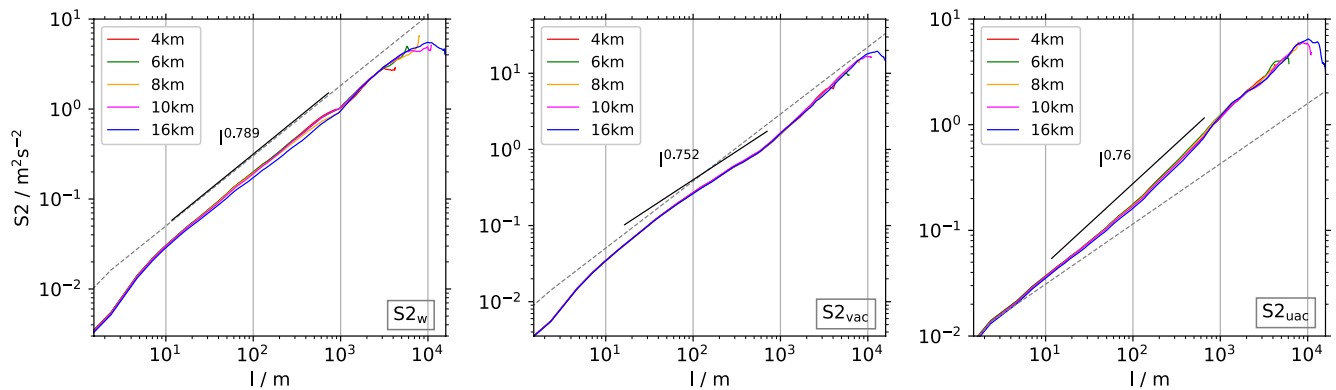
Figure 11. Second-order velocity structure functions on the turbulent subleg calculated using 4, 6, 8, 10, and 16 km subleg lengths for w, vac, and uac (left to right, respectively). As an example, for the sublegs of 4 km, $S2$ is computed in subsets of 4 km, and averaged over all subsets. Inertial range scaling laws inferred from spectral indices are shown as a reference in dotted gray lines. Scaling laws calculated from a best fit in the subinertial range are plotted using black solid lines, along with the obtained values.

$S2 \sim l^{2/3}$. Figure 12 shows the second-order structure functions for w, vac, and uac for the north, center and south patches for different sublegs ranging from 4 to 12 km. Here no color code is used since, as seen for the total turbulent segment, all subleg curves collapse to a single scaling.

Inertial range scaling and indices were calculated based on 4 km sublegs in all cases, so those curves are shown in solid black lines for clarity. Again, the reference scaling is shown in gray dashed lines, and the solid red line is used to show the range of scaling for the calculation of the indices for each component in each segment. In good agreement with the spectra shown in Figure 10, the overall picture shows that there is a transition from the K41 scaling to a steeper inertial range scaling, ranging from $\sim l^{2/3}$ to $\sim l$ for the w and vac velocity components from north to south of the CAT encounter (top to bottom in Figure 12). As seen previously in the spectra, the middle region has a not such a clear scaling (a K41 prediction is given as a reference in this region for uac in Figure 12).

Finally, it is worth mentioning that inertial range scaling for all second-order structure functions satisfy the Monin and Yaglom (1975) conversion law, when applied to the spectral indices of the three wind velocity components on the north, center, and south patches separately. For the south patch, second-order structure functions of w, vac, and uac seem to follow an intermediate inertial range scaling consistent with k^{-2}, which corresponds to $S2 \sim l$. In other words, considering the scaling in each patch separately resolves the apparent contradiction between the scaling of the spectra and the structure functions when the entire CAT event is examined as a whole.

Taking all of these findings into account, the second-order spectra and structure functions on each patch within the CAT encounter describe a region where the flow is more isotropic to the north and more stratified to the south, mediated by a transition region in the center. In this transition region, where elevated EDR values are also observed (albeit to a lesser extent than in the other patches), weaker turbulence is expected, and perhaps structures develop on a shorter scale than in the other two patches.

4.2.2. Third-Order Structure Functions

Figure 13a shows the mixed third-order structure functions $S3$ of uac for the entire turbulence segment calculated using Equation 6 for various sublegs from 4 to 16 km and using the 100 Hz BAHAMAS data. For these curves, sign changes are not considered (note that $S3$, unlike $S2$, is not positive definite), and therefore δuac is replaced by its absolute value in Equation 6. A clear scaling consistent with the 4/3rd law is observed in a range of scales compatible with those observed in $S2$ (the scaling is indicated in Figure 13a as a reference). The same scaling law is also shown as a reference in the signed third-order structure functions for uac, that is, when the signs of δuac are taken into account, see Figure 13b. In the latter case, there are large fluctuations, which is to be expected when higher order moments are computed with a limited number of statistics and also considering that sign changes can lead to cancellations, making the curves more noisy. Since $S3$ is not positive definite, $-S3_{uac}$ is also shown. Remember that the third-order structure function is relevant as it allows direct estimation of the energy flux, and the direction of the cascade.

From here it can be confirmed that, although the CAT event has local structures and bursts with different scalings, the energy cascade evolves from large to small scales throughout the turbulence segment, as the negative
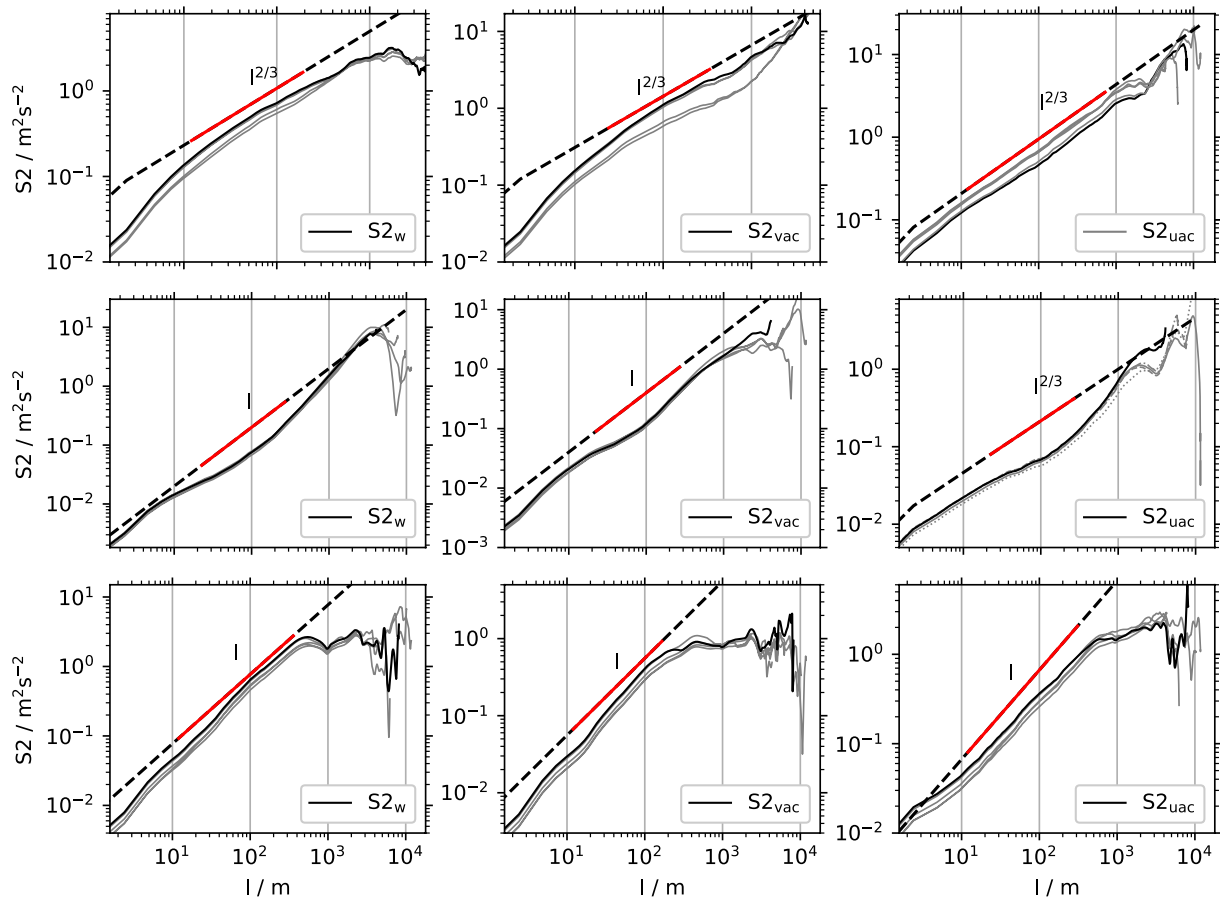
Figure 12. Second-order structure functions for all velocity components in an aircraft-related coordinate system (w, vac, and uac from left to right), calculated for the north patch (top panel), the center patch (middle panel), and the south patch (bottom panel) on the different sublegs considered. Black curves are the second-order structure function obtained for the smaller (4 km) subleg. Reference inertial range scalings are denoted in black dotted lines as a reference. Red solid lines denote the subinertial range scaling used for the calculation of scaling indices according to Equation 5).
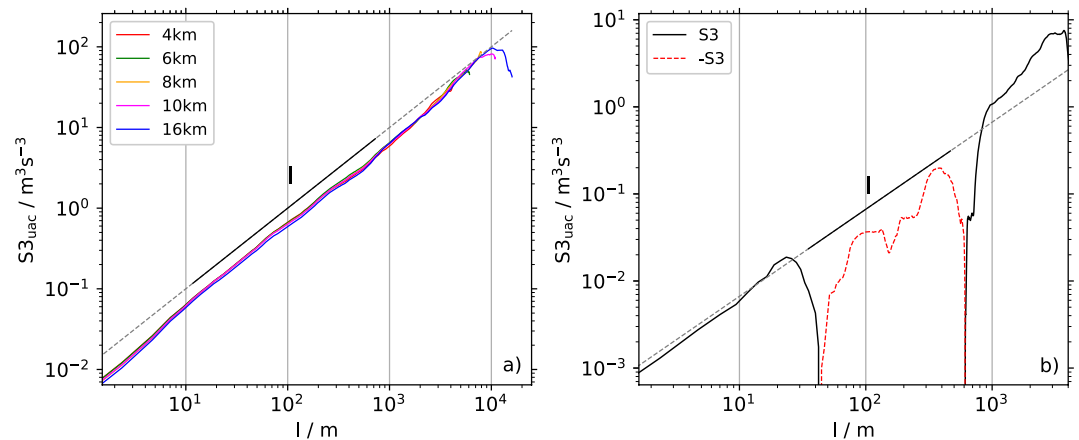

Figure 13. (a) Unsigned mixed third-order velocity structure functions $S3$ according to Equation 6 for horizontal wind component in aircraft-related coordinate system uac, for different subleg lengths. (b) As in panel (a) but taking into account the fluctuations, for a 4 km subleg. The black solid line denotes $S3$, and the red dashed curve is $-S3$. To guide the eye, gray dotted lines show reference scaling from K41, and solid black lines inertial range used for calculations.
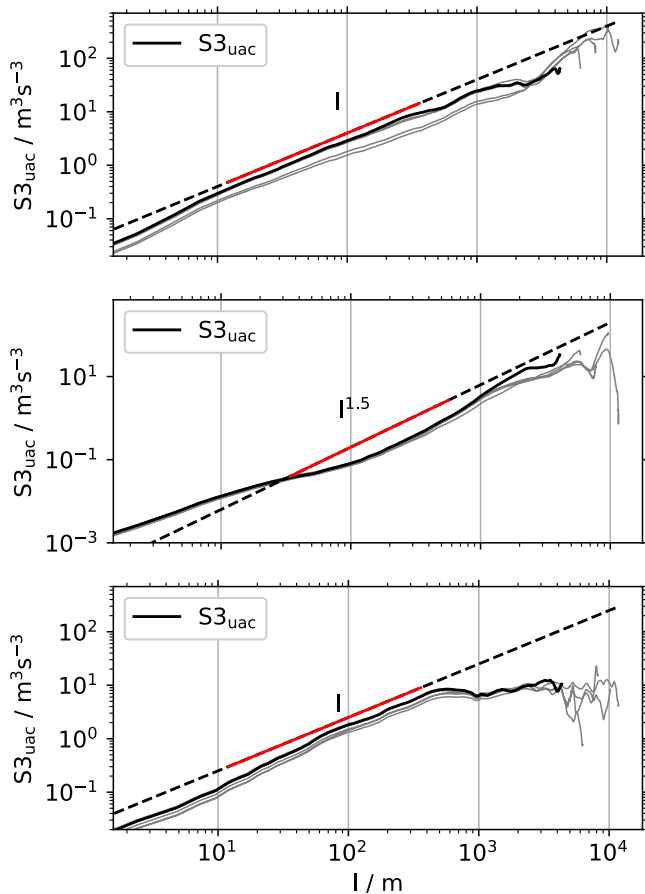
Figure 14. Unsigned mixed third-order velocity structure functions $S3$ according to Equation 6 for horizontal wind component uac in an aircraft-related coordinate system, for different subleg lengths calculated for the north (top panel), center (middle panel) and south (bottom panel) patches. Reference scaling laws are shown in dotted black lines, whereas red solid lines denote the extension of the inertial range used for calculating the scaling indices γ according to Equation (6).

values of $S3$ within the inertial range imply positive values of ϵ and a forward energy cascade. The scaling index γ calculated using the best fit in the identified inertial region for $S3$ (indicated by a solid black line in Figure 13a) is 0.929 ± 0.002.

Figure 14 shows the unsigned, mixed third-order structure functions $S3$ of uac calculated on the different sublegs considered for the north, center, and south patches. The north and south patches display a range of scales compatible with a $\sim l^1$ scaling, while the center patch displays a bumpier structure function with $\sim l^{1.5}$ scaling indicated as a reference. The poor scaling $\gamma \neq 1$ in this patch, together with the behavior of $S2$ and of the spectra, and the smaller EDR, confirm that turbulence is weaker in this transitional patch. In the south patch, $S3$ is compatible with the 4/3 law but displays a plateau for large increments l, which can be associated to gravity waves. This confirms again the picture of two bursty regions in the south and north of the CAT event, with a more isotropic flow in the north, and more stratified turbulence in the south, separated by a transition region.

The third-order structure function $S3$ using Equation 6 provides an independent estimate of the EDR and characteristic length scales, which is independent of the assumption of a Kolmogorov spectral scaling in the turbulent kinetic energy, see Augier et al. (2012) for details. Albeit the signed $S3$ displays strong fluctuations and can thus result in a crude estimate of ϵ, while the unsigned $S3$ can only provide an upper bound for ϵ, they can still be useful considering that the definition of EDR in Equation 3 assumes the spectrum follows K41 scaling. EDR from $S3$ estimated for the entire CAT event yields values of ≈ 0.17 m$^{2/3}$ s^{-1} from the unsigned $S3$ and ≈ 0.07 m$^{2/3}$ s^{-1} from the signed $S3$. These values are consistent with the mean values of EDR for the CAT event estimated from the spectra (see Figure 9). We can also estimate EDR in the north and south patches (the center patch does not display a clear scaling). From the unsigned $S3$, EDR ≈ 0.28 m$^{2/3}$ s^{-1} in the north patch, and ≈ 0.14 m$^{2/3}$ s^{-1} in the south patch (compare with the EDR peaks in Figure 9). Thus, even the south turbulent patch with a steeper energy spectrum seems to be efficient at dissipating energy. Finally, it is worth noting that an estimate of the local buoyancy length scale in the north patch yields ≈ 270 m, a value close to the transition scale from inertial scaling to the plateau in $S3$ in that patch.

5. Discussion

The estimated Froude number, the occurrence of strong bursts of EDR and TKE, and the subsequent transition of spectra for all wind speed components between different regions (patches) within the entire turbulence segment strongly suggest there is large-scale intermittency in the CAT event that HALO experienced. For a more detailed illustration, the left column of Figure 15 shows the EDR values as in Figure 9, but in separate panels for w, vac, and uac. Here, the three identified patches (from north to south) are plotted from right to left in each panel, respectively. The middle column of Figure 15 shows the kurtosis (K) for w, vac, and uac fluctuations (computed over moving windows), and the right column shows a measure of anisotropy calculated in terms of ratios between the velocity fluctuations (from top to bottom, w′/vac′, w′/uac′, and vac′/uac′, respectively).

The kurtosis K measures the deviations from Gaussian statistics, and large positive values indicate that the distribution is characterized by more extreme values. In this way, K quantifies the burstiness of the airflow. Outside the region of the CAT encounter, that is, under relatively smooth flight conditions, the values of K remain close to ≈ 3, in agreement with what would be expected from a Gaussian distribution. Inside the turbulence segment, large spikes of the kurtosis are located at latitudes that correspond to each EDR maxima. For all velocity components, these spikes reach their maximum values south of the CAT event, where the flow is considered more stratified. For the vertical wind velocity fluctuations K reaches values of $K_w \approx 8$, and decreases to peaks of $K_w \approx 6$, around
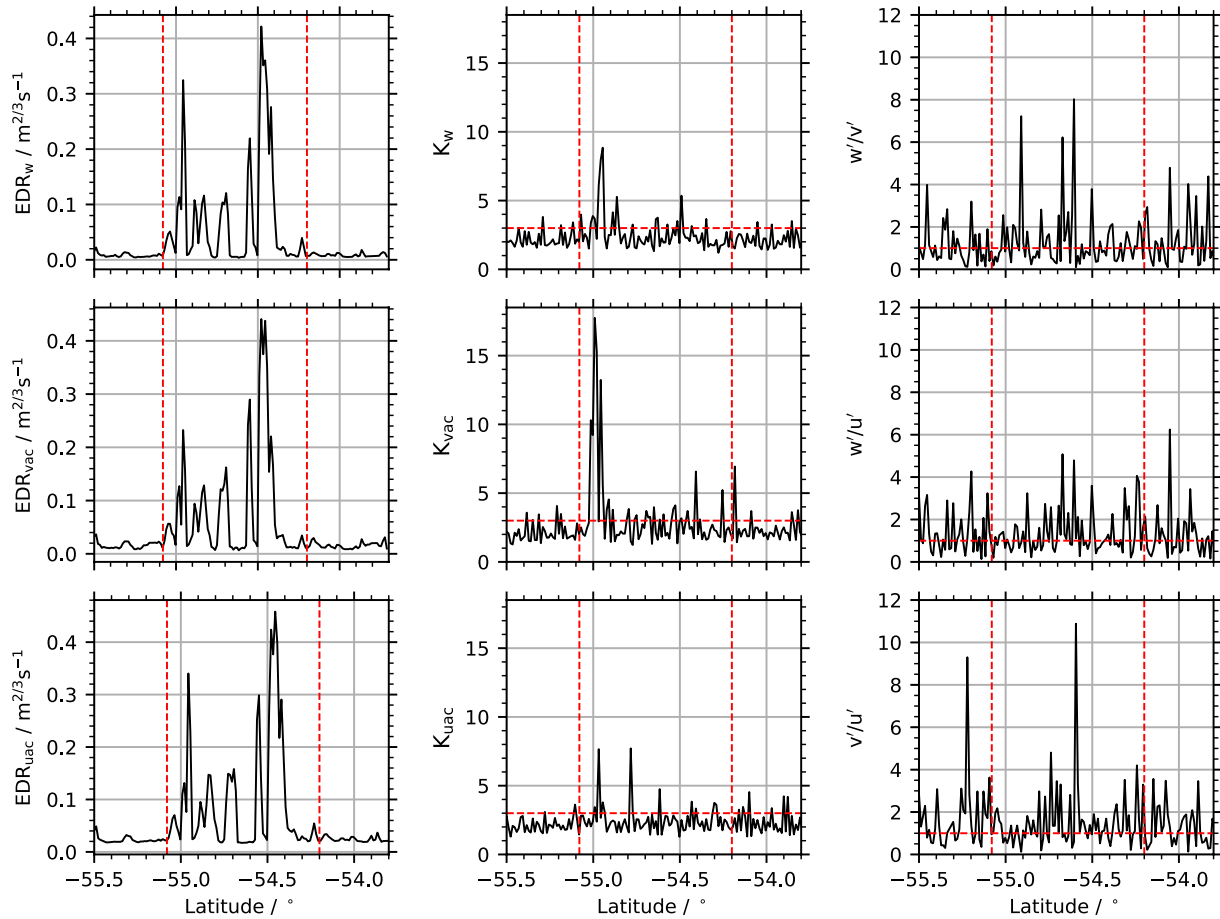
Figure 15. Energy dissipation rate (left column), kurtosis (middle column), and anisotropy measure (right column) as function of latitude for the three velocity components in aircraft-related coordinate system w, vac, uac from top to bottom, respectively. Red vertical lines frame the entire turbulence segment.

both the center and north patches. This decrease in the value of K following the flow recovery to isotropy is observed for the three wind velocity components.

This overall behavior is consistent with the calculated measures of anisotropy: K increases where the flow is more anisotropic. This happens at different rates depending on where (in spatial location) and what (in terms of velocity components) is being compared. North of the CAT event, for example, the three velocity components exhibit similar scaling laws in their spectra and structure functions, consistent with small anisotropy measures. At the same time, these scaling laws are consistent with K41, that is, approximately homogeneous and isotropic turbulence. However, turbulent dissipation occurs in localized regions leading to sudden bursts in the velocity fluctuations and larger values of the kurtosis. South of the CAT event, the flow is more stratified, so increased anisotropy is expected in this region when comparing the vertical to horizontal velocity components (see the w′/uac′ and w′/vac′ panels in Figure 15). Finally, all anisotropy measures show an increase in their values at the center of the CAT event. This is in good agreement with the observations of the second- and third-order structure functions and the spectra, which indicate a very different behavior of w, uac, and vac and a less clear turbulent scaling.

Complementary, this behavior can be interpreted in terms of the buoyancy Reynolds number in each patch, $R_B = Re\, Fr^2 = V^3/(\nu\, N^2\, L) \approx \epsilon/(\nu\, N^2)$, which is a measure of the relative strength of turbulent dissipation to buoyancy. In the turbulent segment, CAT exhibits scaling properties associated with a well-defined energy spectrum and where signatures of anisotropy due to stratification are evident, and therefore a well-defined R_B. In order to maintain this value constant throughout the entire turbulence segment with a locally changing Fr, an increase/decrease in stratification should be followed by a decrease/increase in the corresponding ϵ. This is consistent with results shown in Feraco et al. (2018) and Marino et al. (2022), where it is found that extreme events, such

as bursts in the vertical velocity, are needed when stratification is strong ($Fr \approx 0.1$) for the energy to be locally dissipated as efficiently as in the case of homogeneous and isotropic turbulence at equivalent Reynolds numbers. Similar results follow from derivations of strict scaling laws for stratified turbulence when turbulence is assumed to remain balanced (Augier et al., 2012). Our results show larger EDR values where the flow is closer to isotropy (i.e., where K41 scaling laws hold), indicating that dissipation is more efficient in those regions. On the other hand, K is larger where the flow is more stratified, and where larger departures from Gaussianity are needed to maintain dissipation.

Finally, the description of the dynamics of the turbulent flow in terms of R_B indicates that the observed flow remains in a transitional regime were both eddies and gravity waves are important, highlighting the fact that vertically propagating mountain waves may play a significant role not only in the generation of CAT, but also in its dynamics and evolution. This scenario of interplay between turbulent eddies and gravity waves has been reported in DNSs of stably stratified turbulent flows, see, for example, Rorai et al. (2014), Feraco et al. (2018), and Marino et al. (2022), and in the analysis of observations of the Earth's mesosphere (Chau et al., 2021), see also references therein.

6. Summary and Conclusions

This case study analyzed a CAT event generated by instabilities triggered by the modulation of the ambient flow through vertically propagating mountain waves in the lee of the Southern Andes and north of the Drake passage. Therefore, it is more akin to CAT events that occur in the negative shear above jet streams (Sharman et al., 2012) than those on the anticyclonic side of the jet stream (Knox, 1997). We combined in situ measurements from the research aircraft HALO conducted during the SOUTHTRAC campaign and numerical forecast data to characterize HALO's turbulence encounter. The large-scale and mesoscale atmospheric patterns involved in the CAT generation were analyzed using global and regional numerical models.

The meteorological analysis of the ERA5 data set reveals that an intense high-pressure system located upstream of South America favored southwesterly flow and cold air advection near Tierra del Fuego and south of Santa Cruz during the night of 11 September and early morning hours of 12 September 2019. WRF model data indicate that this airflow over the southern Andes was responsible for the excitation of vertically propagating mountain waves that were refracted southeastward into the core of the jet stream and across HALO's flight track. There, mountain waves modulated the ambient flow such that shear was locally enhanced, resulting in regions of reduced Richardson numbers where instabilities were amplified and turbulence developed.

After describing the meteorological situation, in situ measurements from the Basic HALO Measurement and Sensor System (BAHAMAS) were analyzed using two complementary methods. Spectra as well as structure functions were computed to characterize turbulence on large and small scales. Elevated EDR and TKE values measured at FL400 ($\sim$12 km) during HALO's flight over Tierra del Fuego toward Drake Passage indicates the occurrence of strong turbulence, which agrees well with the timing and location identified in the numerical analysis for possible CAT generation. Both TKE and EDR show multiple peaks within the turbulent segment, with EDR values indicating that HALO experienced moderate-to-severe turbulence, consistent with the pilot's report. The turbulence segment covered a flight distance of about 127 km corresponding roughly to 19% of the entire flight leg 2 of research flight ST08.

The bursty, intermittent nature of the CAT encounter was identified in both TKE and EDR, characterized by multiple peaks occurring in three identified patches within the turbulence segment. In agreement with the DNS results for stably stratified flows of Rorai et al. (2014), Feraco et al. (2018), and Marino et al. (2022), the Froude number determined here is approximately 0.1, indicating that violent turbulence can occur in patches.

A closer inspection of the CAT event reveals large-scale intermittency, possibly generated by the strong correlation observed between the vertical wind velocity and the potential temperature, that is, by the presence of mountain waves. This large-scale intermittency is evidenced by a transition in the inertial range scaling of the wind components between the K41 prediction of $-5/3$ and a steeper spectral of slope of about -2 associated with stratified flow.

Finally, analysis of the kurtosis of the wind velocity components and of anisotropy shows that larger peaks in the kurtosis correspond to increased EDR in the turbulence segment even when the flow is more anisotropic and

stratified. This behavior provides a local balance between dissipation and buoyancy forces within each patch, resulting in a global turbulent dissipation close to that expected from the Kolmogorov prediction, but where signatures of thermal stratification are present when looking at the inertial range scaling of the spectrum and structure functions.

In summary, HALO's turbulence encounter shows that assuming CAT is always Kolmogorov-like, that is, close to isotropic and homogeneous turbulence, and using only global spectral indices to estimate turbulence parameters is a risk, as also discussed by previous authors. Using the unique 100 Hz BAHAMAS measurements during SOUTHTRAC, a bursty behavior was detected for the CAT event studied. In the turbulence segment, there exist regions that nearly scale with Kolmogorov's law and spatially separated regions that have a steeper spectral decay in kinetic energy. This scaling is more consistent with increased thermal stratification, but still allowing turbulent bursts characterized by power laws, enhanced dissipation, and extreme velocity fluctuations. Spectral methods can be useful to study the overall CAT event, but should be used with caution when investigating local properties of atmospheric turbulence as CAT events related to the vertical propagation of mountain waves may present a more patchy nature. Within these patches, which can be some kilometers long, corresponding to only a few minutes of flight time, aircraft can experience periods of stronger/weaker turbulence. In such cases, the usual EDR values predicted based on Kolmogorov theory may not be representative of the actual intensity of CAT experienced. For geographic regions where CAT indices have not yet been calibrated, such as in this case study for the southern tip of South America, the results found here could help in improving calibration and further forecasting capabilities of national weather centers.

Appendix A

Here we present the algorithm implemented to obtain spectra, the α_i, and EDR values by means of Equations 2 and 3 from wind velocity measurements of BAHAMAS. First, the entire leg 2 of length L_0, is subdivided into $l_0 = 4$ km overlapping segments, where individual power spectral densities (PSDs) are calculated following the Welch periodogram method (Welch, 1967). These 4 km segments correspond to time frames
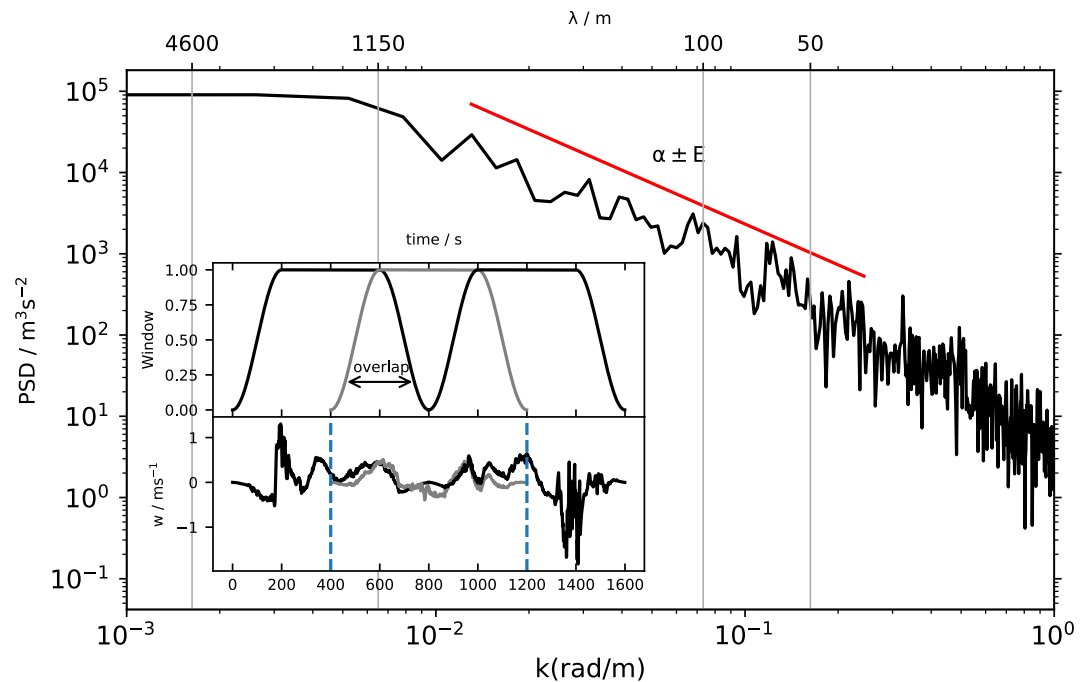

Figure A1. Individual power spectral density of the vertical velocity w obtained from the spectral estimation algorithm applying the Welch method to a 4 km (equivalent to 1,600 points) subleg inside the turbulent segment. Best fit in the selected frequency range is denoted by the red line. Insets show the Tukey window with 50% tapper length and 50% overlap, and the linearly detrended windowed data in the corresponding time frame (in seconds, with count reset to zero). Vertical blue lines in the lowermost inset denote the region where data overlaps.
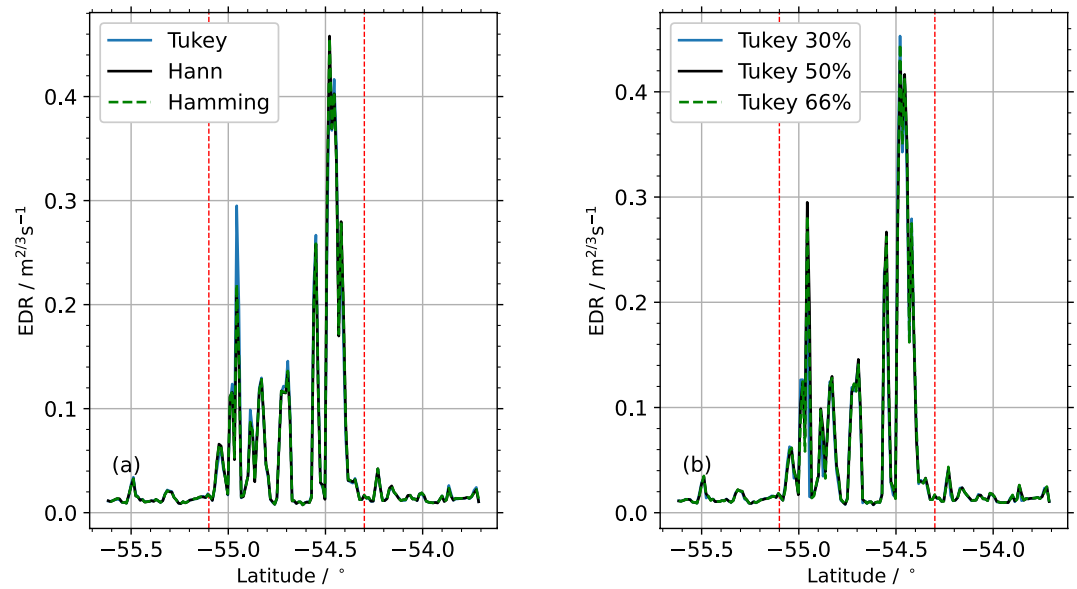
Figure A2. Geometric mean $\overline{\mathrm{EDR}}$ along the flight path derived from 100 Hz BAHAMAS data using; (a) Tukey, Hann, and Hamming windows with 50% overlap, and (b) using Tukey windows with different overlap percentage.

of ≈ 16 s, resulting into $N = 1{,}600$ measured data points (for the frequency $f_s = 100$ Hz). The choice for the length l_0 of these subsegments is based on the following. Segments are intended to be as small as possible, but remaining one order of magnitude larger than the limit imposed by sampling frequency (see below), and also at scales relevant for aircraft (from ~ 100 m to ~ 4 km for most aircraft, Sharman et al. (2014)). On each of these segments, data are linearly detrended, and a windowing procedure is applied before calculating the periodograms. Whereas window selection and overlapping strategies are still widely discussed in the context of spectral methods for data analysis, reported optimal overlap for Welch method lies between 30% and 66%, also applicable for cosine based windowing functions, such as Hann, Hamming, and Tukey windows (see, for instance, Antoni & Schoukens, 2007; Jwo et al., 2019, 2021; Prabhu, 2014). Our final choice after a sensitivity test (see below) was the use of a Tukey window with 50% overlap, that is, periodograms are calculated in subsegments of N/2 data points overlapped by 50%. The 4 km subleg PSDs result from averaging these three periodograms within the N data point segments. Figure A1 shows one of these individual PSDs inside the turbulent segment, with the Tukey window used and the resulting detrended windowed data within the data frames. For each of these 4 km subleg PSDs, the algorithm derives individual energy spectra S_i, individual spectral indices α_i, and EDR point values, rolling on the entire leg of length L_0. Energy spectra are estimated following (Figure A2)

$$S_i = \mathrm{PSD} * \mathrm{ENBW} \tag{A1}$$

where the effective normalized band width (ENBW) for the Tukey window is computed from N, the overlap, and the resolution frequency $f_{\mathrm{res}} = f_s/N$ (for details of the estimations for different windows using the Welch method see, for instance, Heinzel et al. (2002)). The individual spectral indices α_i are obtained from a polynomial fit in log-log scale within a fixed frequency range between 0.24 and 5 Hz, to minimize the squared error

$$E = \sum_{j=1}^{k} |p(f_j) - \mathrm{PSD}(f_j)|^2 \tag{A2}$$

as schematically shown in Figure A1. The distribution of these individual α_i along the turbulence subleg is shown in the histograms of Figure 9 (see the insets). Individual EDR values are those shown in the curves of Figure 10. On the other hand, PSDs of the three wind velocity components shown in the main panels of Figure 9 are the averaged of all 4 km PSDs in the turbulence segment of 127 km. For the calculation of PSDs, S_i, and α_i inside the patches, the algorithm follows the same method inside 4 km segments, where overlapping segments have $N/2$ points.

Here it is very important to note that whereas the fitting errors may be very small, the accuracy of these linear fits is subjected to the variance of the estimated PSDs, which depends on the choice of overlapping and windowing. Due to this, we tested the sensitivity of the spectral estimation algorithm to different windowing techniques and overlapping, on the grounds of similar procedures reported in previous references using aircraft data at similar sampling frequencies (Bramberger et al., 2018, 2020; Strauss et al., 2015).

Whereas overlapping increases statistics and reduces variance, the effect of applying a data window is to suppress spectral leakage due to truncation of the data set. The shortcoming is the loss of resolution due to smearing of peaks (see Prabhu, 2014 and references therein). At the resolutions attained, spectral leakage and signal-to-noise ratio are expected to be similarly mitigated by both Hamming and Hann windowing methods (Jwo et al., 2019 2021), in good agreement with the fact that the Hamming window is 92% a Hann window and 8% a rectangular window. A Tukey window is also a combination of rectangular and Hann windows, depending on the taper length, which in our case is 50%. Whereas Hann windows have low impact on the frequency resolution and good amplitude accuracy of the resulting frequency spectrum (Antoni & Schoukens, 2007; Prabhu, 2014), the advantage of using a Tukey window is the better amplitude accuracy in the frequency domain. In our data, the only substantial difference observed between the use of Hann, Hamming, or Tukey windows was seen in the amplitude of one of the peaks of EDR derived in the turbulence subleg. Figure A2 shows EDR curves (as those from Figure 10) obtained from different windowing and overlapping. In the south patch, the EDR peak reaches a maximum value $\approx 20\%$ smaller for Hann and Hamming windows in contrast with the one obtained using the Tukey window. This difference of 0.06 m$^{2/3}$ s^{-1} is not significant taking into account CAT thresholds reported in Strauss et al. (2015); Bramberger et al. (2018, 2020) and references therein. In addition, our results were tested against EDR values reported in Dörnbrack et al. (2022) derived using an independent algorithm for the same data set. Finally, the choice of Blackman windowing was discarded based on the larger information lost in comparison with Hann type windows. Other methods more computationally expensive (like those based on Bessel functions) were also discarded.

Data Availability Statement

The observational data from the BAHAMAS sensor are freely available at https://doi.org/10.5281/zenodo.6918363. The WRF fields used to create Figure 5 are also uploaded there. In addition, the BAHAMAS data are stored in the HALO database https://halo-db.pa.op.dlr.de/mission/116. ECMWF ERA5 data are available via the ECMWF web page https://www.ecmwf.int/en/forecasts/datasets/reanalysis-datasets/era5.

References

Alexandrova, O., Carbone, V., Veltri, P., & Sorriso-Valvo, L. (2008). Small-scale energy cascade of the solar wind turbulence. *The Astrophysical Journal*, *674*(2), 1153–1157. https://doi.org/10.1086/524056

Antoni, J., & Schoukens, J. (2007). A comprehensive study of the bias and variance of frequency-response-function measurements: Optimal window selection and overlapping strategies. *Automatica*, *43*(10), 1723–1736. https://doi.org/10.1016/j.automatica.2007.02.020

Antonia, R. A., Ould-Rouis, M., Anselmet, F., & Zhu, Y. (1997). Analogy between predictions of Kolmogorov and Yaglom. *Journal of Fluid Mechanics*, *332*, 395–409. https://doi.org/10.1017/S0022112096004090

Antonia, R. A., Tang, S. L., Djenidi, L., & Zhou, Y. (2019). Finite Reynolds number effect and the 4/5 law. *Physical Review Fluids*, *4*(8), 084602. https://doi.org/10.1103/PhysRevFluids.4.084602

Augier, P., Galtier, S., & Billant, P. (2012). Kolmogorov laws for stratified turbulence. *Journal of Fluid Mechanics*, *709*, 659–670. https://doi.org/10.1017/jfm.2012.379

Bacmeister, J. T., Schoeberl, M. R., Lait, L. R., Newman, P. A., & Gary, B. (1990). ER-2 mountain wave encounter over Antarctica: Evidence for blocking. *Geophysical Research Letters*, *17*(1), 81–84. https://doi.org/10.1029/GL017i001p00081

Bramberger, M., Dörnbrack, A., Wilms, H., Ewald, F., & Sharman, R. (2020). Mountain-wave turbulence encounter of the research aircraft HALO above Iceland. *Journal of Applied Meteorology and Climatology*, *59*(3), 567–588. https://doi.org/10.1175/JAMC-D-19-0079.1

Bramberger, M., Dörnbrack, A., Wilms, H., Gemsa, S., Raynor, K., & Sharman, R. (2018). Vertically propagating mountain waves—A hazard for high-flying aircraft? *Journal of Applied Meteorology and Climatology*, *57*(9), 1957–1975. https://doi.org/10.1175/JAMC-D-17-0340.1

Carli, B., Cortesi, U., Blom, C. E., Chipperfield, M. P., Rossi, G. D., & Redaelli, G. (2000). Airborne polar experiment Geophysica aircraft in Antarctica (APE-GAIA). *SPARC Newsletter*, *15*, 21–24.

Champagne, F. H. (1978). The fine-scale structure of the turbulent velocity field. *Journal of Fluid Mechanics*, *86*(1), 67–108. https://doi.org/10.1017/S0022112078001019

Chau, J. L., Marino, R., Feraco, F., Urco, J. M., Baumgarten, G., Lübken, F.-J., et al. (2021). Radar observation of extreme vertical drafts in the polar summer mesosphere. *Geophysical Research Letters*, *48*, e2021GL094918. https://doi.org/10.1029/2021GL094918

Cho, J. Y. N., & Lindborg, E. (2001). Horizontal velocity structure functions in the upper troposphere and lower stratosphere: 1. Observations. *Journal of Geophysical Research*, *106*(D10), 10223–10232. https://doi.org/10.1029/2000JD900814

Cho, J. Y. N., Newell, R. E., Anderson, B. E., Barrick, J. D. W., & Thornhill, K. L. (2003). Characterizations of tropospheric turbulence and stability layers from aircraft observations. *Journal of Geophysical Research*, *108*(D20), 8784. https://doi.org/10.1029/2002JD002820

Cornman, L. B. (2016). Airborne in situ measurements of turbulence. In R. Sharman, & T. Lane (Eds.), *Aviation turbulence: Processes, detection, prediction* (pp. 97–120). Springer International Publishing. https://doi.org/10.1007/978-3-319-23630-8_5

Cornman, L. B., Morse, C. S., & Cunning, G. (1995). Real-time estimation of atmospheric turbulence severity from in-situ aircraft measurements. *Journal of Aircraft*, *32*(1), 171–177. https://doi.org/10.2514/3.46697

Davidson, P. (2022). *Turbulence: An introduction for scientist and engineers*. Oxford University Press. https://doi.org/10.1093/acprof:oso/9780198722588.001.0001

Dörnbrack, A., Bechtold, P., & Schumann, U. (2022). High-resolution aircraft observations of turbulence and waves in the free atmosphere and comparison with global model predictions. *Journal of Geophysical Research: Atmospheres*, *127*, e2022JD036654. https://doi.org/10.1029/2022JD036654

Dörnbrack, A., Kaifler, B., Kaifler, N., Rapp, M., Wildmann, N., Garhammer, M., et al. (2020). Unusual appearance of mother-of-pearl clouds above El Calafate, Argentina (50° 21′S, 72° 16′W). *Weather*, *75*(12), 378–388. https://doi.org/10.1002/wea.3863

Doyle, J. D., Shapiro, M. A., Jiang, Q., & Bartels, D. L. (2005). Large-amplitude mountain wave breaking over Greenland. *Journal of the Atmospheric Sciences*, *62*(9), 3106–3126. https://doi.org/10.1175/JAS3528.1

Dudhia, J. (1989). Numerical study of convection observed during the winter monsoon experiment using a mesoscale two-dimensional model. *Journal of the Atmospheric Sciences*, *46*(20), 3077–3107. https://doi.org/10.1175/1520-0469(1989)046<3077:NSOCOD>2.0.CO;2

Eliassen, A., & Palm, E. (1960). On the transfer of energy in stationary mountain waves. *Geofysiske Publikasjoner*, *22*(3), 1–23.

Ellrod, G., Lester, P. F., & Ehernberger, L. J. (2003). Clear air turbulence. In J. R. Holton (Ed.), *Encyclopedia of atmospheric sciences* (pp. 393–403). Academic Press. https://doi.org/10.1016/B0-12-227090-8/00104-4

Essenwanger, O., & Reiter, E. R. (1969). Power spectrum, structure function, vertical wind shear, and turbulence in troposphere and stratosphere. *Archiv für Meteorologie, Geophysik und Bioklimatologie, Serie A*, *18*(1–2), 17–24. https://doi.org/10.1007/BF02247861

Feraco, F., Marino, R., Pumir, A., Primavera, L., Mininni, P. D., Pouquet, A., & Rosenberg, D. (2018). Vertical drafts and mixing in stratified turbulence: Sharp transition with Froude number. *Europhysics Letters*, *123*(4), 44002. https://doi.org/10.1209/0295-5075/123/44002

Ferreira, D., Marshall, J., Bitz, C. M., Solomon, S., & Plumb, A. (2015). Antarctic Ocean and sea ice response to ozone depletion: A two-time-scale problem. *Journal of Climate*, *28*(3), 1206–1226. https://doi.org/10.1175/JCLI-D-14-00313.1

Frisch, U. (1995). *Turbulence*. Cambridge University Press.

Gary, B. L. (2008). Mesoscale temperature fluctuations in the Southern Hemisphere stratosphere. *Atmospheric Chemistry and Physics*, *8*(16), 4677–4681. https://doi.org/10.5194/acp-8-4677-2008

Giez, A., Mallaun, C., Nenakhov, V., & Zöger, M. (2021). *Calibration of a Nose Boom mounted airflow sensor on an atmospheric research aircraft by Inflight Maneuvers (Tech. Rep. No. 2021-17)*. DLR. Retrieved from https://elib.dlr.de/145704/

Giez, A., Mallaun, C., Zöger, M., Dörnbrack, A., & Schumann, U. (2017). Static pressure from aircraft trailing-cone measurements and numerical weather-prediction analysis. *Journal of Aircraft*, *54*(5), 1728–1737. https://doi.org/10.2514/1.C034084

Gottlieb, D., & Orszag, S. A. (1977). *Numerical analysis of spectral methods*. Society for Industrial and Applied Mathematics. https://doi.org/10.1137/1.9781611970425

Gultepe, I., Sharman, R., Williams, B., Zhou, P. D., Ellrod, G., Minnis, P., et al. (2019). A review of high impact weather for aviation meteorology. *Pure and Applied Geophysics*, *176*(5), 1869–1921. https://doi.org/10.1007/s00024-019-02168-6

Heinzel, G., Rüdiger, A., & Schilling, R. (2002). Spectrum and spectral density estimation by the Discrete Fourier transform (DFT), including a comprehensive list of window functions and some new at-top windows. *Forschungspapier*. Retrieved from https://hdl.handle.net/11858/00-001M-0000-0013-557A-5

Hersbach, H., Bell, B., Berrisford, P., Hirahara, S., Horányi, A., Muñoz-Sabater, J., et al. (2020). The ERA5 global reanalysis. *Quarterly Journal of the Royal Meteorological Society*, *146*(730), 1999–2049. https://doi.org/10.1002/qj.3803

Hoblit, F. M. (1988). *Gust loads on aircraft: Concepts and applications*. American Institute of Aeronautics and Astronautics, Inc. (AIAA Education Series). https://doi.org/10.2514/4.861888

Holland, M. M., Landrum, L., Kostov, Y., & Marshall, J. (2017). Sensitivity of Antarctic sea ice to the Southern Annular Mode in coupled climate models. *Climate Dynamics*, *49*(5–6), 1813–1831. https://doi.org/10.1007/s00382-016-3424-9

Hong, S.-Y., & Lim, J.-O. J. (2006). The WRF single-moment 6-class microphysics scheme (WSM6). *Asia-Pacific Journal of Atmospheric Sciences*, *42*(2), 129–151.

Janić, Z. I. (2001). *Nonsingular implementation of the Mellor-Yamada level 2.5 scheme in the NCEP Meso model*. US Department of Commerce, National Oceanic and Atmospheric Administration.

Jucker, M., & Goyal, R. (2022). Ozone-forced southern annular mode during Antarctic stratospheric warming events. *Geophysical Research Letters*, *49*, e2021GL095270. https://doi.org/10.1029/2021GL095270

Jwo, D.-J., Chang, W.-Y., & Wu, I.-H. (2021). *Windowing techniques, the welch method for improvement of power spectrum estimation*. CMC-COMPUTERS MATERIALS & CONTINUA.

Jwo, D.-J., Wu, I.-H., & Chang, Y. (2019). Windowing design and performance assessment for mitigation of spectrum leakage. *E3s Web of Conferences*, *94*, 03001.

Knox, J. A. (1997). Possible mechanisms of clear-air turbulence in strongly anticyclonic flows. *Monthly Weather Review*, *125*(6), 1251–1259. https://doi.org/10.1175/1520-0493(1997)125<1251:PMOCAT>2.0.CO;2

Koch, S. E., Jamison, B. D., Lu, C., Smith, T. L., Tollerud, E. I., Girz, C., et al. (2005). Turbulence and gravity waves within an upper-level front. *Journal of the Atmospheric Sciences*, *62*(11), 3885–3908. https://doi.org/10.1175/JAS3574.1

Kolmogorov, A. N. (1941a). The local structure of turbulence in incompressible viscous fluid for very large Reynolds numbers. *Doklady Akademii Nauk SSSR*, *30*, 301–305.

Kolmogorov, A. N. (1941b). Dissipation of energy in locally isotropic turbulence. *Doklady Akademii Nauk SSSR*, *32*, 16–18.

Lane, T. P., Sharman, R. D., Trier, S. B., Fovell, R. G., & Williams, J. K. (2012). Recent advances in the understanding of near-cloud turbulence. *Bulletin of the American Meteorological Society*, *93*(4), 499–515. https://doi.org/10.1175/bams-d-11-00062.1

Lesieur, M. (1993). Understanding coherent vortices through computational fluid dynamics. *Theoretical and Computational Fluid Dynamics*, *5*(4–5), 177–193. https://doi.org/10.1007/BF00271657

Lilly, D. K. (1978). A severe downslope windstorm and aircraft turbulence event induced by a mountain wave. *Journal of the Atmospheric Sciences*, *35*(1), 59–77. https://doi.org/10.1175/1520-0469(1978)035<0059:ASDWAA>2.0.CO;2

Lindborg, E. (1999). Can the atmospheric kinetic energy spectrum be explained by two-dimensional turbulence? *Journal of Fluid Mechanics*, *388*, 259–288. https://doi.org/10.1017/S0022112099004851

MacCready, P. B. (1964). Standardization of Gustiness values from aircraft. *Journal of Applied Meteorology and Climatology*, *3*(4), 439–449. https://doi.org/10.1175/1520-0450(1964)003<0439:SOGVFA>2.0.CO;2

Mahrt, L. (1989). Intermittency of atmospheric turbulence. *Journal of the Atmospheric Sciences*, *46*(1), 79–95. https://doi.org/10.1175/1520-0469(1989)046<0079:IOAT>2.0.CO;2

Marino, R., Feraco, F., Primavera, L., Pumir, A., Pouquet, A., Rosenberg, D., & Mininni, P. D. (2022). Turbulence generation by large-scale extreme vertical drafts and the modulation of local energy dissipation in stably stratified geophysical flows. *Physical Review Fluids*, *7*(3), 033801. https://doi.org/10.1103/physrevfluids.7.033801

Mazon, J., Rojas, J., Lozano, M., Pino, D., Prats, X., & Miglietta, M. (2018). Influence of meteorological phenomena on worldwide aircraft accidents, 1967–2010. *Meteorological Applications*, *25*(2), 236–245. https://doi.org/10.1002/met.1686

McCann, D. W. (2001). Gravity waves, unbalanced flow, and aircraft clear air turbulence. *National Weather Digest*, *25*(1/2), 3–14.

Mlawer, E. J., Taubman, S. J., Brown, P. D., Iacono, M. J., & Clough, S. A. (1997). Radiative transfer for inhomogeneous atmospheres: RRTM, a validated correlated-k model for the longwave. *Journal of Geophysical Research*, *102*(D14), 16663–16682. https://doi.org/10.1029/97JD00237

Monin, A. S., & Yaglom, A. M. (1975). *Statistical fluid mechanics, Vol. I: Mechanics of turbulence* (1st ed.). MIT Press.

Mukul Tewari, N., Tewari, M., Chen, F., Wang, W., Dudhia, J., LeMone, M., et al. (2004). Implementation and verification of the unified NOAH land surface model in the WRF model (Formerly Paper Number 17.5). In *20th conference on weather analysis and forecasting/16th conference on numerical weather prediction* (pp. 11–15). American Meteorological Society.

Oncley, S. P., Friehe, C. A., Larue, J. C., Businger, J. A., Itsweire, E. C., & Chang, S. S. (1996). Surface-layer fluxes, profiles, and turbulence measurements over uniform terrain under near-neutral conditions. *Journal of the Atmospheric Sciences*, *53*(7), 1029–1044. https://doi.org/10.1175/1520-0469(1996)053<1029:SLFPAT>2.0.CO;2

Panofsky, H. A., Dutton, J. A., Hemmerich, K. H., McCreary, G., & Loving, N. V. (1968). Case studies of the distribution of CAT in the troposphere and stratosphere. *Journal of Applied Meteorology and Climatology*, *7*(3), 384–389. https://doi.org/10.1175/1520-0450(1968)007<0384:CSOTDO>2.0.CO;2

Parish, T. R., & Bromwich, D. H. (1989). Instrumented aircraft observations of the katabatic wind regime near terra nova bay. *Monthly Weather Review*, *117*(7), 1570–1585. https://doi.org/10.1175/1520-0493(1989)117<1570:IAOOTK>2.0.CO;2

Pearson, B., & Fox-Kemper, B. (2018). Log-normal turbulence dissipation in global ocean models. *Physical Review Letters*, *120*(9), 094501. https://doi.org/10.1103/PhysRevLett.120.094501

Piper, M., & Lundquist, J. K. (2004). Surface layer turbulence measurements during a frontal passage. *Journal of the Atmospheric Sciences*, *61*(14), 1768–1780. https://doi.org/10.1175/1520-0469(2004)061<1768:SLTMDA>2.0.CO;2

Powers, J. G., Klemp, J. B., Skamarock, W. C., Davis, C. A., Dudhia, J., Gill, D. O., et al. (2017). The weather research and forecasting model: Overview, system efforts, and future directions. *Bulletin of the American Meteorological Society*, *98*(8), 1717–1737. https://doi.org/10.1175/BAMS-D-15-00308.1

Prabhu, K. (2014). *Window functions and their applications in signal processing*. CRC Press.

Rapp, M., Kaifler, B., Dörnbrack, A., Gisinger, S., Mixa, T., Reichert, R., et al. (2021). SOUTHTRAC-GW: An airborne field campaign to explore gravity wave dynamics at the World's strongest hotspot. *Bulletin of the American Meteorological Society*, *102*(4), E871–E893. https://doi.org/10.1175/BAMS-D-20-0034.1

Rodriguez Imazio, P., Dörnbrack, A., Urzua, R. D., Rivaben, N., & Godoy, A. (2022). Clear air turbulence observed across a tropopause fold over the Drake passage—A case study. *Journal of Geophysical Research: Atmospheres*, *127*, e2021JD035908. https://doi.org/10.1029/2021JD035908

Rorai, C., Mininni, P. D., & Pouquet, A. (2014). Turbulence comes in bursts in stably stratified flows. *Physical Review E: Statistical Physics, Plasmas, Fluids, and Related Interdisciplinary Topics*, *89*(4), 043002. https://doi.org/10.1103/PhysRevE.89.043002

Schmid, H., & Dörnbrack, A. (1999). Simulation of breaking gravity waves during the south Foehn of January 7–13, 1996. *Contributions to Atmospheric Physics*, *72*(4), 287–301.

Sharman, R. D., Cornman, L. B., Meymaris, G., Pearson, J., & Farrar, T. (2014). Description and derived Climatologies of Automated in situ eddy-dissipation-rate reports of atmospheric turbulence. *Journal of Applied Meteorology and Climatology*, *53*(6), 1416–1432. https://doi.org/10.1175/jamc-d-13-0329.1

Sharman, R. D., Trier, S. B., Lane, T. P., & Doyle, J. D. (2012). Sources and dynamics of turbulence in the upper troposphere and lower stratosphere: A review. *Geophysical Research Letters*, *39*, L12803. https://doi.org/10.1029/2012GL051996

Skabar, Y. G., Matsudo, C., Sacco, M., Ruiz, J. J., & Righetti, S. (2018). *Implementación modelo de pronóstico numérico WRF*. Repositorio Institucional Servicio Meteorológico Nacional. Retrieved from https://repositorio.smn.gob.ar/bitstream/handle/20.500.12160/631/Nota_Tecnica_SMN_2018-45.pdf?sequence=1%26isAllowed=y

Skamarock, W. C., & Klemp, J. B. (2008). A time-split nonhydrostatic atmospheric model for weather research and forecasting applications. *Journal of Computational Physics*, *227*(7), 3465–3485. https://doi.org/10.1016/j.jcp.2007.01.037

Smalikho, J. (1997). Accuracy of the turbulent energy dissipation rate estimation from the temporal spectrum of wind velocity fluctuations. *Atmospheric and Oceanic Optics*, *10*, 559–563.

Smith, R. B., & Kruse, C. G. (2017). Broad-spectrum mountain waves. *Journal of the Atmospheric Sciences*, *74*(5), 1381–1402. https://doi.org/10.1175/JAS-D-16-0297.1

Smith, R. B., Nugent, A. D., Kruse, C. G., Fritts, D. C., Doyle, J. D., Eckermann, S. D., et al. (2016). 07) stratospheric gravity wave fluxes and scales during DEEPWAVE. *Journal of the Atmospheric Sciences*, *73*(7), 2851–2869. https://doi.org/10.1175/JAS-D-15-0324.1

Strauss, L., Serafin, S., Haimov, S., & Grubišić, V. (2015). Turbulence in breaking mountain waves and atmospheric rotors estimated from airborne in situ and Doppler radar measurements. *Quarterly Journal of the Royal Meteorological Society*, *141*(693), 3207–3225. https://doi.org/10.1002/qj.2604

Tuck, A. F. (2008). *Atmospheric turbulence: A molecular dynamics perspective* (1st ed.). Oxford University Press.

Tuck, A. F. (2021). Perspective on aircraft in the stratosphere: 50 Years from COMESA through the ozone Hole to climate. *Quarterly Journal of the Royal Meteorological Society*, *147*(735), 713–727. https://doi.org/10.1002/qj.3958

Tuck, A. F., Brune, W. H., & Hipskind, R. S. (1997). Airborne southern Hemisphere ozone experiment/measurements for Assessing the effects of stratospheric aircraft (ASHOE/MAESA): A road map. *Journal of Geophysical Research*, *102*(D3), 3901–3904. https://doi.org/10.1029/96JD02745

Tuck, A. F., Watson, R. T., Condon, E. P., Margitan, J. J., & Toon, O. B. (1989). The planning and execution of ER-2 and DC-8 aircraft flights over Antarctica, August and September 1987. *Journal of Geophysical Research*, *94*(D9), 11181–11222. https://doi.org/10.1029/JD094iD09p11181

Večenaj, Z., Belušić, D., Grubišić, V., & Grisogono, B. (2012). Along-coast features of Bora-related turbulence. *Boundary-Layer Meteorology*, *143*(3), 527–545. https://doi.org/10.1007/s10546-012-9697-6

Vinnichenko, N. (1980). *Turbulence in the free atmosphere* (1st ed.). Springer Verlag. https://doi.org/10.1007/978-1-4757-0100-5

Wacławczyk, M., Gozingan, A. S., Nzotungishaka, J., Mohammadi, M., & P. Malinowski, S. (2020). Comparison of different techniques to calculate properties of atmospheric turbulence from low-resolution data. *Atmosphere*, *11*(2), 199. https://doi.org/10.3390/atmos11020199

Watkins, C., & Browning, K. (1973). The detection of clear air turbulence by radar. *Physics in Technology*, *4*(1), 28–61. https://doi.org/10.1088/0305-4624/4/1/i01

Welch, P. (1967). The use of fast Fourier transform for the estimation of power spectra: A method based on time averaging over short, modified periodograms. *IEEE Transactions on Audio and Electroacoustics*, *15*(2), 70–73. https://doi.org/10.1109/TAU.1967.1161901

Wildmann, N., Eckert, R., Dörnbrack, A., Gisinger, S., Rapp, M., Ohlmann, K., & van Niekerk, A. (2021). In situ measurements of wind and turbulence by a Motor glider in the Andes. *Journal of Atmospheric and Oceanic Technology*, *38*(4), 921–935. https://doi.org/10.1175/JTECH-D-20-0137.1

Williams, P. D., Haine, T. W., & Read, P. L. (2005). On the generation mechanisms of short-scale unbalanced modes in rotating two-layer flows with vertical shear. *Journal of Fluid Mechanics*, *528*, 1–22. https://doi.org/10.1017/s0022112004002873

Williams, P. D., Haine, T. W., & Read, P. L. (2008). Inertia-gravity waves emitted from balanced flow: Observations, properties, and consequences. *Journal of the Atmospheric Sciences*, *65*(11), 3543–3556. https://doi.org/10.1175/2008jas2480.1

Williams, P. D., Read, P., & Haine, T. (2003). Spontaneous generation and impact of inertia-gravity waves in a stratified, two-layer shear flow. *Geophysical Research Letters*, *30*(24), 2255. https://doi.org/10.1029/2003GL018498

Wilms, H., Bramberger, M., & Dörnbrack, A. (2020). Observation and simulation of mountain wave turbulence above Iceland: Turbulence intensification due to wave interference. *Quarterly Journal of the Royal Meteorological Society*, *146*(732), 3326–3346. https://doi.org/10.1002/qj.3848